J. Adv. Model. Earth Syst., **Vol. 000**, Art. #2011ms000081, 21 pp.

JAMES
JOURNAL OF ADVANCES IN MODELING EARTH SYSTEMS

# A mechanism denial study on the Madden-Julian Oscillation

*Daehyun Kim*[1], *Adam H. Sobel*[1,2,3] *and In-Sik Kang*[4]

[1] Lamont-Doherty Earth Observatory, Earth Institute at Columbia University, 61 Rte. 9W, Palisades, NY 10964, USA.
[2] Department of Applied Physics and Applied Mathematics, Columbia University, New York, New York, USA.
[3] Department of Earth and Environmental Sciences, Columbia University, New York, New York, USA.
[4] School of Earth and Environmental Sciences, Seoul National University, San 56-1, Sillim-dong, Gwanak-gu, Seoul 154–747, South Korea.

A series of Madden-Julian oscillation (MJO) mechanism-denial experiments is performed using an atmospheric general circulation model (AGCM). Daily climatological seasonal cycles of i) surface latent heat flux, ii) net radiative heating rate, and iii) surface wind stress are obtained from a control simulation and prescribed in place of the normal interactive computations of these fields in order to turn off the i) wind-induced surface heat exchange (WISHE), ii) cloud-radiation interaction (CRI), and iii) frictional wave-CISK (FWC) mechanisms, respectively. Dual and triple mechanism denial experiments are also conducted by switching off multiple mechanisms together. The influence of each mechanism is assessed by comparing experiments with that mechanism turned off to those in which it is not. CRI and WISHE are both found to be important to the simulated MJO amplitude and propagation speed, while FWC has weaker and less systematic effects. The MJO is weakened when CRI is turned off, but strengthened when WISHE is turned off, indicating that CRI amplifies the MJO in the control simulation while WISHE weakens it. The negative influence of WISHE is shown to result from simulated phase relationships between surface winds, surface fluxes and convection which differ significantly from those found in observations, and thus is not interpreted as evidence against a positive role for WISHE in the development and maintenance of the observed MJO. The positive influence of CRI in the model is consistent with a strong simulated relationship between daily grid-point column-integrated radiative and convective heating; the mean ratio of the latter to the former exceeds 0.2 for rain rates less than 14 mm d$^{-1}$. CRI is also shown to suppress an excessive excitation of the convectively coupled Kelvin wave so that the amplitude and frequency of the MJO is maintained.

DOI:

## 1. Introduction

The Madden-Julian oscillation (MJO) [*Madden and Julian*, 1971, 1972] is the dominant mode of tropical intraseasonal variability, characterized by its planetary spatial scale, 30–60 day period, and eastward propagation. By modulating deep convection over the tropics, the MJO has large impacts on a wide variety of climate phenomena across different spatial and temporal scales. Some examples include the onset and break of the Indian and Australian summer monsoons [e.g., *Yasunari*, 1979; *Wheeler and McBride*, 2005], the formation of tropical cyclones [e.g., *Liebmann and Hartmann*, 1984; *Maloney and Hartmann*, 2000a, 2000b; *Bessafi and Wheeler*, 2006] and the onset of some El Nino events [e.g., *Kessler et al.*, 1995; *Moore and Kleeman*, 1999; *Takayabu et al.*, 1999; *Bergman et al.*, 2001; *Kessler*, 2001].

Theories have been suggested based on observations and model results to explain the existence of the MJO and its characteristics, particularly its spatial and temporal scales and propagation direction. Below we introduce some of these theories, particularly those relevant to our study. Readers are referred to reviews by *Zhang* [2005], *Wang* [2005], and *Waliser* [2006] for more complete reviews of MJO theories.

In the mobile wave-CISK (conditional instability of second kind) theory [*Lau and Peng*, 1987], the eastward propagating intraseasonal variability in the tropics was hypothesized to result from selective amplification of low-wavenumber Kelvin waves. Indeed, the phase speed of the eastward propagating, large-scale wave of *Lau and Peng* [1987] is close to that of convectively coupled equatorial

**To whom correspondence should be addressed.**
D. Kim, Lamont-Doherty Earth Observatory, Earth Institute at Columbia University, 61 Rte. 9W, Palisades, NY 10964, USA.
(dkim@ldeo.columbia.edu)



**Journal of Advances in Modeling Earth Systems 2011ms000081.3d** 28/11/11 16:41:31
*The Charlesworth Group*, Wakefield +44(0)1924 369598 - Rev 7.51n/W (Jan 20 2003)

Kelvin waves [*Wheeler and Kiladis*, 1999], but faster than that of the MJO. In frictional wave-CISK (FWC) theory [*Wang*, 1988a; *Salby et al.*, 1994], friction in the boundary layer results in coupling between the moist Kelvin and Rossby modes [*Wang and Rui*, 1990]. This moist Kelvin-Rossby coupled wave packet favors planetary scales, slower eastward propagation, and suppression of the uncoupled moist Kelvin mode [*Wang and Rui*, 1990]. The FWC theory has been supported by several observational studies [*Hendon and Salby*, 1994; *Jones and Weare*, 1996; *Maloney and Hartmann*, 1998; *Matthews*, 2000] and modeling studies [*Lau and Lau*, 1986; *Lau and Chan*, 1988; *Sperber et al.*, 1997; *Waliser et al.*, 1999; *Lee et al.*, 2003].

In the wind-evaporation feedback or wind induced surface heat exchange (WISHE) theory [*Emanuel*, 1987; *Neelin et al.*, 1987], the destabilization of the convectively coupled Kelvin wave is driven by anomalous latent heat flux at the surface induced by anomalous wind speed. The anomalous wind speed results when easterly wind anomalies due to the wave are superimposed on an assumed basic state easterly wind. The anomalously strong easterlies and fluxes lie to the east of the convection maximum. This shifts the convection eastward, so that the convective heating becomes partly in phase with positive temperature anomalies, resulting in generation of available potential energy. This theory, however, has been shown to be inconsistent with the observed MJO in some respects. Those are: i) the theory assumes mean easterlies while mean zonal wind is westerly in the region (i.e., equatorial Indian ocean and west Pacific during boreal winter) where the MJO is active [e.g., *Wang*, 1988b], and ii) observations show that anomalous evaporation is strongest to the west of the convection, not to the east as suggested by WISHE theory [*Shinoda et al.*, 1998]. Nonetheless, these are only weaknesses with the original specific linear form of the theory, rather than with the general notion of surface fluxes as destabilizing the MJO. In fact some evidence from observations and numerical simulations supports the proposition that surface fluxes play an important role [e.g., *Sobel et al.*, 2008, 2010], though the details of the mechanism must differ from that in the original linear theory. Positive feedback from surface heat flux anomalies is also crucial in destabilization of some modes in the more recent idealized model studies of *Fuchs and Raymond* [2002, 2005, 2007].

Local radiative-convective feedback has also been proposed as a mechanism for generating intraseasonal disturbances [*Hu and Randall*, 1994, 1995; *Waliser*, 1996; *Raymond*, 2001; *Fuchs and Raymond*, 2002, 2005, 2007; *Sobel and Gildor*, 2003; *Stephens et al.*, 2004]. Additional radiative heating due to the greenhouse effect of high convective clouds is hypothesized to destabilize large-scale disturbances, such as the MJO. While the radiative heating is a small fraction of the convective heating - about 10∼15%, according to *Lin and Mapes* [2004] – the radiative heating is a net source of moist static energy or moist entropy, whereas the convective heating is not. Radiative and surface fluxes have this in common, being the primary sources of moist static energy or moist entropy; the hypothesis that these two processes are important amounts to a hypothesis that the MJO is fundamentally a diabatic phenomenon, rather than a moist adiabatic one. The similarity between radiative-convective and surface turbulent flux feedbacks goes further, as the total (shortwave plus longwave) radiative effects of high clouds tend to cool the surface by an amount comparable to their heating of the atmosphere, so that in the column integral they behave similarly to a surface flux [*Sobel and Gildor*, 2003; *Sobel et al.*, 2008, 2010].

It would be easy to test the importance of one mechanism if we could turn it off in nature. Of course, this is not possible. Despite the efforts described above (and others), there is yet no satisfactory and broadly agreed-upon theory for the MJO. Perhaps for related reasons, numerical simulation of the MJO has been a difficult test for most climate models [*Slingo et al.*, 1996; *Lin et al.*, 2006], although recent modeling studies have reported greater success in MJO simulations [*Benedict and Randall*, 2009; *Maloney*, 2009]. *Lin et al.* [2006[] showed that only 2 models in the Third Coupled Model Intercomparison Project (CMIP3) had MJO variance comparable to observations, with even those lacking realism in many other MJO features. At the same time, however, many previous studies have shown that simulation of the MJO can achieve performance better than that shown by *Lin et al.* [2006[ by changing aspects of the cumulus parameterization of the GCM. The methods used include employing mechanisms to inhibit parameterized cumulus convection [*Tokioka et al.*, 1988; *Wang and Schlesinger*, 1999; *Lee et al.*, 2003; *Lin et al.*, 2008], improved representations of downdrafts and rain re-evaporation [*Maloney and Hartmann*, 2001], and modified convective closures [*Zhang and Mu*, 2005].

Although there are several known ways to improve the MJO in model simulations, there have been limited attempts to understand the improvement of a GCM simulation in the frameworks of the above-mentioned theories. When we change a convection scheme so that the simulated MJO strengthens, what is the macroscopic mechanism by which that simulated MJO is initiated and maintained? We apply the adjective ‘‘macroscopic’’ when referring to mechanisms such as those described above – WISHE, radiative-convective feedbacks, frictional wave-CISK etc. – to indicate that these are processes that emerge holistically from the physics and dynamics and act (according to the various hypotheses) to drive the MJO. This is distinct from processes that are explicitly represented within the physical parameterizations, such as entrainment, downdrafts, rain re-evaporation, and others. More is known about how these ‘‘microscopic’’ processes can be manipulated in convective parameterizations to control MJO amplitude in a model than about which macroscopic mechanisms – those which are most explicitly discussed in theoretical work – act to generate the MJO in those comprehensive models which do simulate it with at least moderate success.



Journal of Advances in Modeling Earth Systems 2011ms000081.3d 28/11/11 16:41:32
*The Charlesworth Group*, Wakefield +44(0)1924 369598 - Rev 7.51n/W (Jan 20 2003)

We aim to identify the macroscopic mechanisms which are most important to the simulated MJO in one particular model. We also address the extent to which the model's simulations of the MJO itself, as well as key details of some of the specific mechanisms, are realistic compared to observations. If we could go on to answer these questions in a wide range of models with varying degrees of fidelity in their MJO simulations, we might be able to use our growing capability to simulate the MJO numerically in the service of greater understanding of its large-scale dynamics.

The simplest and most direct way to determine the importance of a given mechanism in a model is to disable it, and then ask to what extent its removal adversely affects the simulated MJO. Following *Neelin et al.* [1987], *Maloney and Sobel* [2004] and *Sobel et al.* [2010] tested WISHE theory by using specified, non-interactive surface wind speeds in the calculations of surface latent heat flux. Those studies found (in two different GCMs, respectively) that the amplitude of the MJO was reduced significantly when WISHE was suppressed. To turn off cloud-radiation interaction (CRI), *Lee et al.* [2001] prescribed the zonal mean net radiative heating rate in place of the interactively-computed one in an aqua-planet framework. They found that longwave-cumulus anvil cloud interaction had negative effects on tropical ISO simulation by effectively exciting small-scale disturbances continuously. *Grabowski* [2003] investigated the role of WISHE and CRI mechanisms in the development and maintenance of MJO-like disturbance simulated by using the cloud-resolving convection parameterization. In his results, WISHE was shown to have a moderate importance in the development of the MJO-like disturbance, while CRI played a minor role. *Chao and Chen* [2001] turned off FWC in their model simulating MJO by replacing wind stress with its zonal mean value at each time step. They found that disabling FWC did not significantly affect the MJO in their model. Despite the above examples, there has been no systematic study in which multiple different mechanisms have been tested in one single model. In the current study, we conducted a series of MJO mechanism-denial experiments in a systematic way using one AGCM. The tested mechanisms are i) WISHE, ii) CRI, and iii) FWC.

Section 2 describes the model used, experimental designs, and the data used for validation. The results from the MJO mechanism-denial experiments are shown and discussed in Section 3. Conclusions are given in section 4.

## 2. Model, Experimental Design, and Data

### 2.1. Atmospheric General Circulation Model

The model used in this study is the Seoul National University (SNU) AGCM. The model is a global spectral model, with 20 vertical levels in sigma coordinates. In this study, T42 ($\sim$2.8°x2.8°) truncation is used for the model's horizontal resolution. The standard deep convection scheme of the SNU AGCM is a simplified version of the Relaxed Arakawa-Schubert (RAS) [*Moorthi and Suarez*, 1992] scheme by *Numaguti et al.* [1995]. Major simplifications and differences from the original Arakawa–Schubert scheme [*Arakawa and Schubert*, 1974] are described in detail in *Numaguti et al.* [1995] and *Lee et al.* [2003]. The large-scale condensation scheme consists of a prognostic microphysics parameterization for total cloud liquid water [*Le Treut and Li*, 1991] with a diagnostic cloud fraction parameterization. A nonprecipitating shallow convection scheme [*Tiedtke*, 1984] is also implemented in the model for mid-tropospheric moist convection. The boundary layer scheme is a nonlocal diffusion scheme based on *Holtslag and Boville* [1993], while the land surface model is from *Bonan* [1996]. Radiation is parameterized by the two-stream k-distribution scheme implemented by *Nakajima et al.* [1995].

### 2.2. Experimental Design

The cumulus parameterization simulates a spectrum of convective plumes at every time step. Each convective plume has its own entrainment rate, which represents the rate at which the rising cloud plume is diluted by environmental air. Given the properties of parcel at cloud base, and environmental (i.e., grid-mean) thermodynamic conditions in a column, which are the same for all plumes, the cloud top for a given plume becomes lower when its entrainment rate is larger. The Tokioka modification [*Tokioka et al.*, 1988], which suppresses convective plumes with entrainment rates less than a threshold that varies inversely with planetary boundary layer (PBL) depth, is implemented in the SNU AGCM. The minimum threshold value is defined as $\mu_{min}=\alpha/D$, where D is the depth of the planetary boundary layer (PBL) and alpha is a non-negative constant. The constant $\alpha$, which determines the minimum entrainment rate for a given PBL depth, is set to 0 and 0.1 in Tok0 and Tok0.1 experiments, respectively. The value $\alpha=0.1$ is sufficiently large that the Tokioka modification inhibits deep plumes significantly in the presence of typical PBL depths.

A series of MJO mechanism-denial experiments is conducted with Tok0.1, by prescribing one or more model variables that are obtained from Tok0.1 using the climatology for each variable in place of its normal interactively-determined value. Surface evaporation, net radiative heating rate, and surface wind stress (in both zonal and meridional direction) are prescribed, to turn off WISHE, CRI, and FWC, respectively. For example, the surface evaporation does not interact with surface winds when we prescribe it, thereby we can effectively switch off WISHE. For each mechanism denial experiment we replace the interactive variables in question with zonally asymmetric, daily- and annually-varying climatologies constructed from the control run, in order to change the mean state as little as possible from that run. In single mechanism denial experiments, only one variable is prescribed, while multiple mechanisms are switched off together in double and triple mechanism denial experiments. All experiments conducted in this study are



Journal of Advances in Modeling Earth Systems 2011ms000081.3d 28/11/11 16:41:32
The Charlesworth Group, Wakefield +44(0)1924 369598 - Rev 7.51n/W (Jan 20 2003)

summarized in Table 1. The double and triple mechanism denial experiments are useful in that they provide more samples with which to examine the impact of each mechanism. For example, the effect of CRI can be evaluated by comparing Tok0.1 and noC (because all mechanism denial experiments are using Tok0.1, we omit the label Tok0.1 when we mention the mechanism denial experiments), as well as noW and noW/C, noF and noC/F, and noW/F and noW/C/F. In all noF (no FWC) experiments, zonal and meridional surface wind stresses are prescribed only between 30°S-30°N. The values from the control experiment are used as they are between 20°S-20°N, but are combined linearly with the interactively calculated value in remaining area. The fraction of the prescribed value in the combination is one in 20°S/N and linearly decreasing with latitude to zero at 30°S/N. Each version is integrated with observed monthly SST, which is used for the second phase of the atmospheric model intercomparison project, for the period of 1979–2005 as a lower boundary condition.

### 2.3. Data

We validate the simulations of rainfall against the Global Precipitation Climatology Project (GPCP) dataset [*Huffman et al.*, 2001]. We use outgoing longwave radiation (OLR) from the Advanced Very High Resolution Radiometer (AVHRR) [*Liebmann and Smith*, 1996]. The upper (200-hPa) and lower (850-hPa) tropospheric zonal winds are from National Centers for Environmental Prediction (NCEP)–National Center for Atmospheric Research (NCAR) reanalysis data [*Kalnay et al.*, 1996]. For the surface latent heat flux we also use the objectively analyzed air–sea fluxes (OAFlux) from *Yu and Weller* [2007]. The structures of specific humidity and 925-hPa moisture convergence based on the 40-yr European Centre for Medium-Range Weather Forecasts (ECMWF) ReAnalysis (ERA-40) [*Uppala et al.*, 2005] are included in our analysis since *Tian et al.* [2006] indicated possible shortcomings in the MJO-relevant specific humidity fields from the NCEP–NCAR reanalysis.

## 3. Results

### 3.1. Mean, ISV, and Eastward Propagation of ISV

November-April time-averaged precipitation and 850-hPa zonal wind are drawn in Figure 1 from observations and all simulations conducted in this study as described in Section 2. In observations (Figure 1a), the climatological boreal winter precipitation over the Pacific is characterized by maxima on the west and east sides of the intertropical convergence zone (ITCZ), and in the south Pacific convergence zone (SPCZ). A salient feature over the Indian Ocean is the east-west asymmetry, with a maximum in the eastern side. Along the equator, the region of eastward 850-hPa zonal wind, bounded by thick solid line in Figure 1, elongates from the western Indian Ocean to the date line. The presence, extent and strength of mean westerlies over the western Pacific have been suggested as indicators of the ability of a model to represent the MJO in that region [e.g., *Inness et al.*, 2003; *Sperber et al.*, 2005].

The observed rainfall maxima are generally well captured in the two control simulations (Tok0 and Tok0.1). Compared to Tok0 (Figure 1f), however, Tok0.1 (Figure 1b) simulates more rainfall in the SPCZ and Indian Ocean, and less (but closer to the observed magnitude) in the western ITCZ. The mean state changes apparent here from Tok0 to Tok0.1 are common features in AGCMs when a change to a given model is made such that the simulated MJO becomes stronger [*Kim et al.*, 2011]. Note that the simulations shown by *Kim et al.* [2011] include the two control simulations here, with lengthened simulation period (20 years). The mean westerlies over the western Pacific are stronger and extend further to the east in Tok0.1 than Tok0, while the westerlies over the Indian Ocean are weakened in Tok0.1.

It seems from Figure 1 that the patterns of mean precipitation in the mechanism denial simulations are more similar to those of Tok0.1 than to those of Tok0. In other words, the changes in the mean state caused by prescribing variables in order to turn off feedbacks in a single model version are smaller than the differences between different versions. We infer from this that any changes in the characteristics of the simulated MJO can be mostly attributed to the direct effects of internal processes on MJO dynamics, rather than to indirect impacts through the mean state. There are, however, some systematic differences in the mean states in the various mechanism denial experiments. When the interaction between the surface wind and evaporation is turned off (e.g., Tok0.1 vs. noW, noC vs. noW/C, noF vs. noW/F, and noC/F vs. noW/C/F), the region of mean westerlies becomes wider in the meridional direction over the western Pacific. Equatorial precipitation is also

**Table 1.** Description of Mechanism-Denial Experiments[a]

| | Tok0/Tok0.1 | No W | No C | No F | No W/C | No W/F | No C/F | No W/C/F |
|---|---|---|---|---|---|---|---|---|
| WISHE | on | off | on | on | off | off | on | off |
| CRI | on | on | off | on | off | on | off | off |
| FricCISK | on | on | on | off | on | off | off | off |

[a]WISHE (W): wind-induced surface heat exchange; CRI (C): cloud-radiation interaction; FricCISK (F): frictional wave-CISK. In no F experiments, zonal and meridional surface wind stresses are prescribed only between 30°S-30°N. Value from control experiment is used as it is between 20°S-20°N, while it is mixed with calculated value in remaining area. The fraction of prescribed value in the mixture is one in 20°S/N and linearly decreasing with latitude to zero at 30°S/N.



Journal of Advances in Modeling Earth Systems 2011ms000081.3d 28/11/11 16:41:33
*The Charlesworth Group*, Wakefield +44(0)1924 369598 - Rev 7.51n/W (Jan 20 2003)

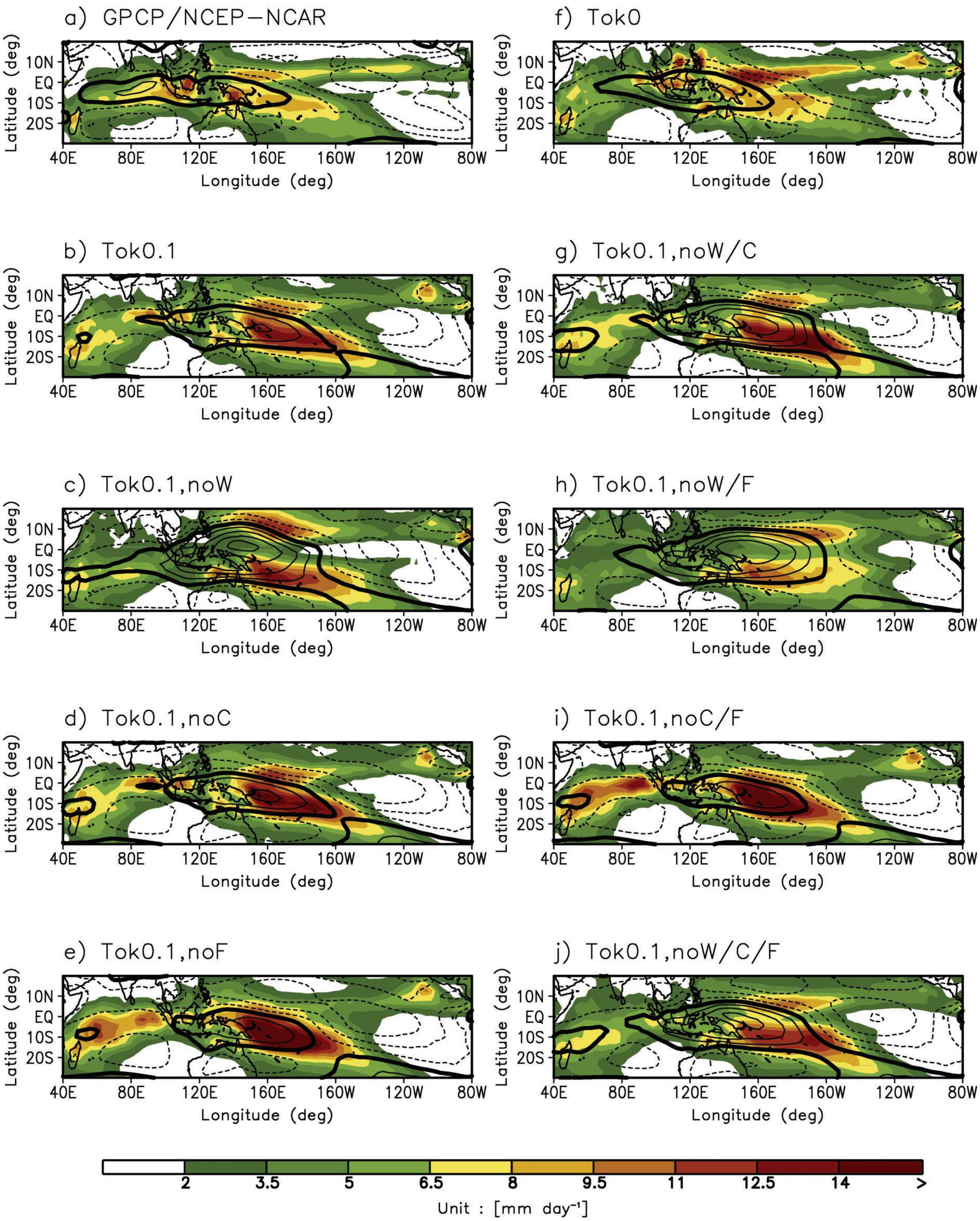


**Figure 1.** November–April mean precipitation (mm day$^{-1}$) (shaded) and 850-hPa zonal wind (m s$^{-1}$) (contoured) of (a) GPCP/NCEP-NCAR, (b) Tok0.1, (c) Tok0.1,noW, (d) Tok0.1,noC, (e) Tok0.1,noF, (f) Tok0, (g) Tok0.1,noW/C, (h) Tok0.1,noW/F, (i) Tok0.1,noC/F, and (j) Tok0.1,noW/C/F. Contours of mean 850-hPa zonal wind are plotted every 3 m s$^{-1}$ with the zero line represented by a thick solid line.

reduced, resulting in a double ITCZ in the western Pacific. When the surface wind interacts with evaporation, variability of the surface wind and evaporation increases when at the same time surface momentum damping is disabled (e.g., Tok0.1 vs. noF, noC vs. noC/F). This increase of variability occurs mainly over the Indian Ocean and SPCZ region (not shown) where mean precipitation also increases, suggesting the role of evaporation variability on the pattern of mean



**Journal of Advances in Modeling Earth Systems 2011ms000081.3d** 28/11/11 16:41:33
*The Charlesworth Group*, Wakefield +44(0)1924 369598 - Rev 7.51n/W (Jan 20 2003)

precipitation. Determining the reasons for these changes in the mean state without WISHE and FWC is beyond the scope of the current study.

In Figure 2, maps of sub-seasonal (20-100-day bandpass filtered) variance of precipitation and 850-hPa zonal wind, observed and simulated, are displayed. The patterns and magnitudes of precipitation variability generally follow those of the mean, except over the islands of the Maritime continent. Over those islands, there is no maximum - as there is in mean precipitation - in the magnitude of ISV,

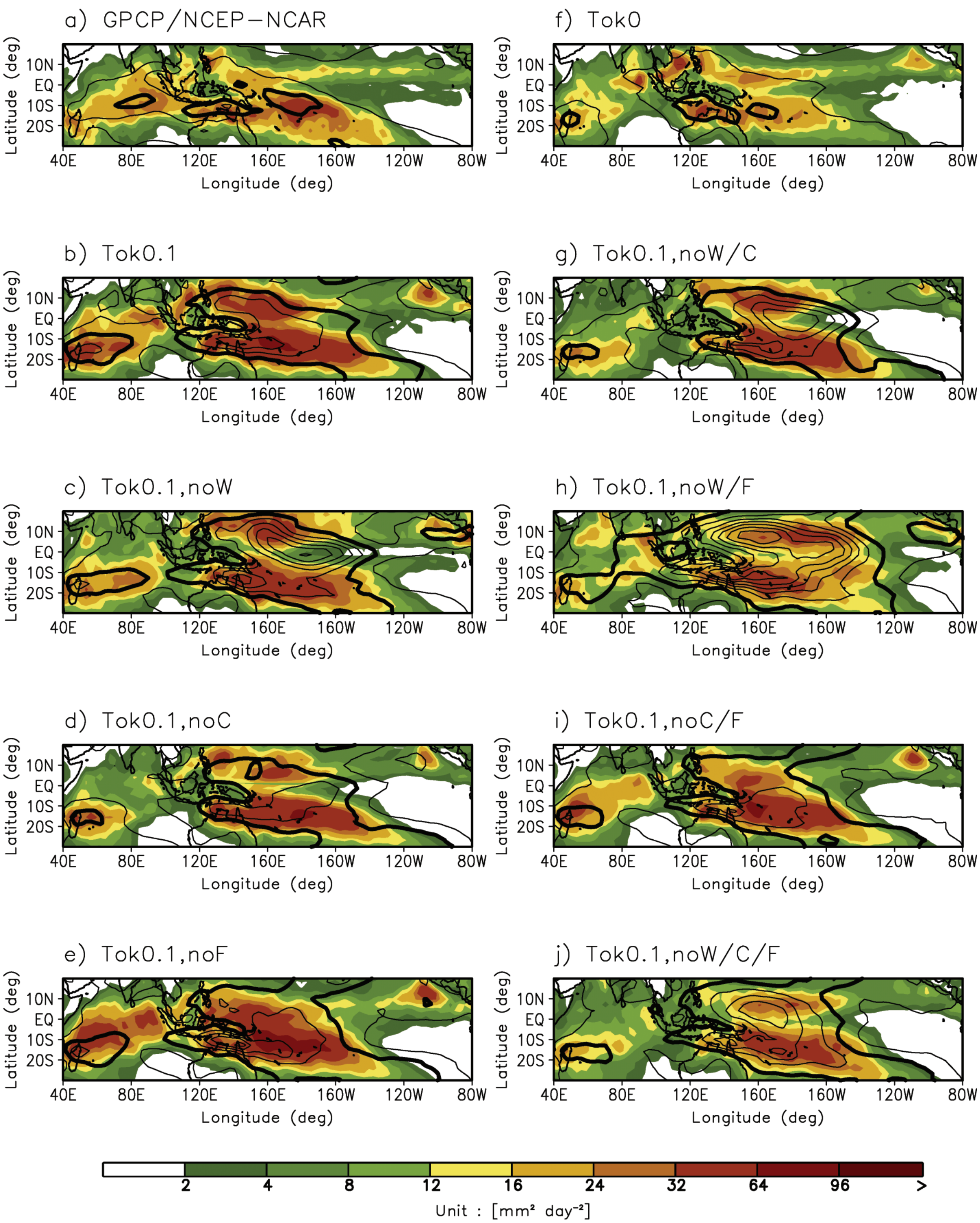


**Figure 2.** As in Figure 1 but for variance of 20–100-day bandpass filtered precipitation (mm$^2$ day$^{-2}$) and 850-hPa zonal wind (m$^2$ s$^{-2}$). Contours of 850-hPa zonal wind variance are plotted every 5 m$^2$ s$^{-2}$ with the 10 m$^2$ s$^{-2}$ line represented by the thick solid line.



**Journal of Advances in Modeling Earth Systems 2011ms000081.3d** 28/11/11 16:41:54
*The Charlesworth Group*, Wakefield +44(0)1924 369598 - Rev 7.51n/W (Jan 20 2003)

suggesting the role of total surface heat flux in generating or maintaining ISV [*Sobel et al.*, 2008, 2010]. In contrast to precipitation, the variance of 20-100-day filtered 850-hPa zonal wind generally doesn't have the same structure as does its mean. It rather follows the pattern of precipitation variance, implying strong local coupling between precipitation and lower level zonal wind variability on the sub-seasonal time scale.

Tok0.1 features stronger ISV of both precipitation and 850 hPa zonal wind than does either Tok0 or observations. When surface latent heat flux is prescribed, the pattern of variance broadens in the meridional direction, which is consistent with the change in the mean state. Turning off CRI reduces the amplitude of sub-seasonal variability. This implies that CRI plays a significant role in generating or maintaining the ISV of precipitation, which in turn is tightly coupled to that of 850 hPa zonal wind. In contrast, sub-seasonal variability is strengthened when the zonal and meridional surface wind stresses are prescribed. When the surface drag does not depend on the instantaneous wind speed, the distribution of wind speeds becomes broader - the slow winds become slower and the fast winds become faster. The surface thermodynamic fluxes depend on the instantaneous winds (apart from the noW/F simulation), so the surface fluxes become more variable as well. The variability in surface latent heat flux is dramatically enhanced in both of total and intraseasonal time scale in noF compared to that in Tok0.1 (not shown). This suggests that the increase of sub-seasonal variability in noF may be due in part to the increase of surface flux variability in that run.

Figure 3 shows lag-correlation coefficients of 10°S-10°N averaged, 20-100-day filtered 850-hPa zonal wind anomalies against a reference time series constructed by averaging the same anomaly data over the Indian Ocean (75-90°E, 5°S-5°N). When we compare the two control simulations, the observed eastward propagation of lower-tropospheric zonal wind anomaly is better simulated in Tok0.1 than Tok0, as shown by *Lin et al.* [2008], and *Kim et al.* [2011]. When the mechanism denial experiments are compared, it is found that the eastward propagation becomes stronger without WISHE (Tok0.1 vs. noW, noC vs. noW/C, noF vs. noW/F), except when all three mechanisms are turned off (noC/F vs. noW/C/F). This implies that interactive surface flux has negative effects on the generation of eastward-propagating ISV, i.e., it hinders the simulated MJO rather than strengthening it. We will show in the next section that this results from simulated phase relationships between surface winds, surface fluxes and precipitation that are significantly different than those found in observations. CRI, on the other hand, appears to have major positive effects on the simulated MJO; the eastward propagation weakens significantly without CRI (Tok0.1 vs. noC, noW vs. noW/C, noF vs. noC/F, and noW/F vs. noW/C/F). The interaction between cloud and radiation seems to play a crucial role in the generation of intraseasonal variability in general, and the eastward-propagating MJO in particular. When FWC is switched off, on the other hand, it seems that changes in characteristics of the eastward propagation are not systematic.

To quantify the relative importance of each mechanism, we develop some simple measures of ISV amplitude and propagation. We can then compare how much those measures change when each individual mechanism, and combination of mechanisms, is disabled. As gross measures of amplitude and eastward propagation of the ISV in each simulation, we choose tropics-averaged standard deviation of 20-100-day filtered anomaly and eastward/westward ratio, respectively. The eastward/westward ratio is defined as the sum of eastward propagating spectral power with wavenumbers from 1 to 3 and periods from 30 to 70 days, divided by its westward propagating counterpart.

Figure 4 shows a scatter plot of the amplitude of ISV in precipitation and the eastward/westward ratio of 850-hPa zonal wind. In Figure 4, closed squares show observation (black), Tok0 (blue), and Tok0.1 (red). Open squares, open diamonds, and crosses represent the simulations without WISHE, CRI, and FWC, respectively. Combinations of symbols represent double or triple mechanism denial experiments. All mechanism denial experiments are in red to represent they are based on Tok0.1. To distinguish simulations that have similar values of the metrics from each other, we zoom in and show a subset of the experiments in the inset of Figure 4. The most notable feature in Figure 4 is the difference between symbols that do or do not have an open diamond, but are otherwise the same; this difference indicates the role of CRI. Whenever CRI is turned off in this model, the amplitude of ISV becomes weaker and its eastward propagation becomes less prominent. Turning off the FWC (cross symbol) enhances ISV amplitude without a clear change in eastward propagation. Switching off WISHE tends to increase the eastward/westward ratio. These conclusions are consistent to those drawn from the preceding figures (e.g. Figure 3), suggesting the usefulness of this kind of metric to diagnose characteristics of ISV simulated in models.

### 3.2. Combined EOF Approach

The impacts of each mechanism on the simulated MJO are investigated in this section using diagnostics intended to extract the MJO more specifically, as opposed to just the magnitude and tendency to eastward propagation of ISV. For this purpose, it is necessary to extract the MJO in observations and simulations, to compare them with each other. The MJO is defined here as the leading mode of coherent variability between anomalies in OLR and those in upper and lower tropospheric zonal wind. We adopt the combined empirical orthogonal function (CEOF) approach [*Wheeler and Hendon*, 2004] for this purpose. Unlike *Wheeler and Hendon* [2004], in which unfiltered anomalies are used because real-time applicability is one of the most important concerns in their study, we use 20-100-day filtered 850 and



**Journal of Advances in Modeling Earth Systems 2011ms000081.3d** 28/11/11 16:42:10
*The Charlesworth Group*, Wakefield +44(0)1924 369598 - Rev 7.51n/W (Jan 20 2003)

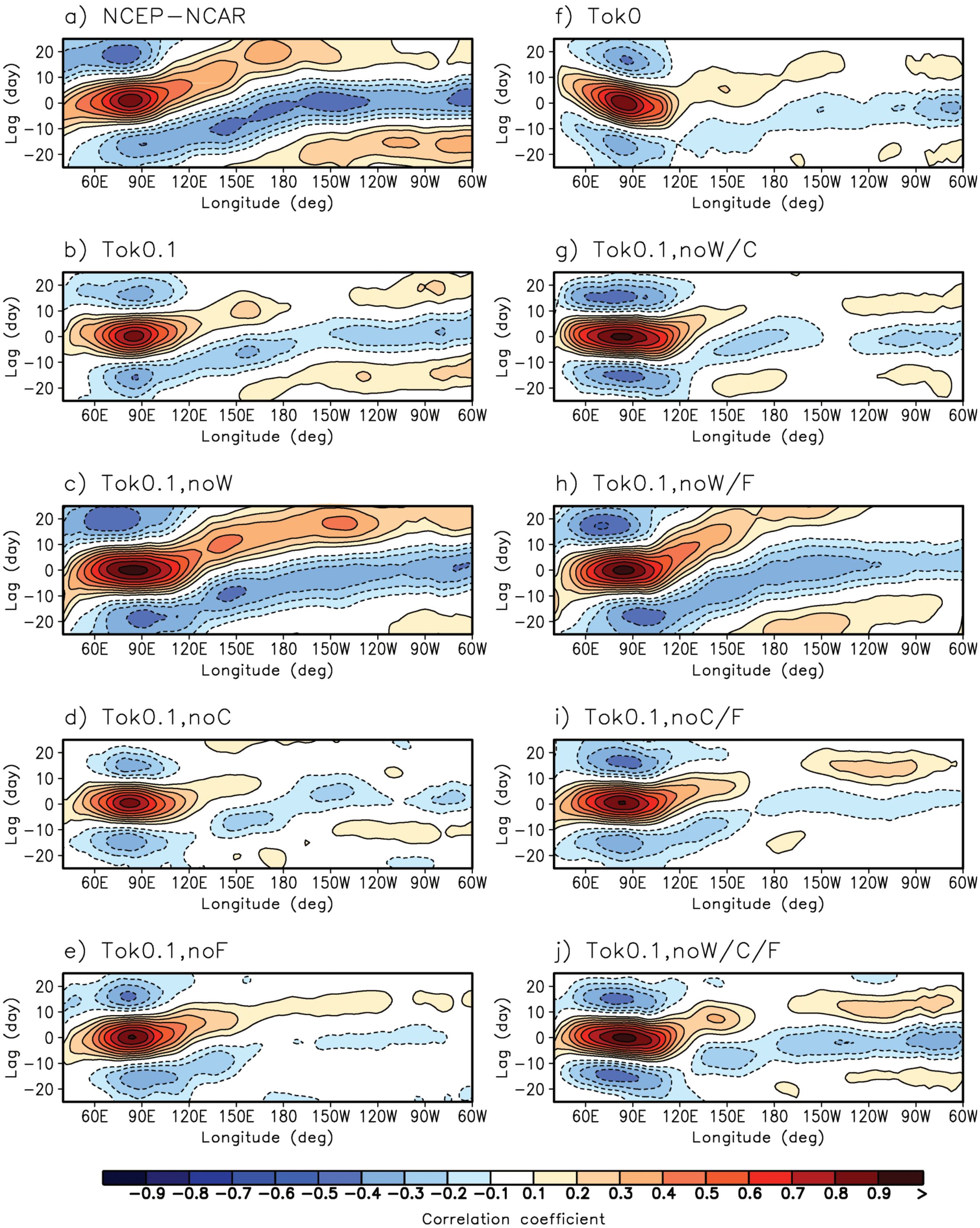


**Figure 3.** As in Figure 1 but for November-April lag-longitude diagram of 10°N-10°S averaged intraseasonal 850-hPa zonal wind anomalies correlated against intraseasonal zonal wind anomalies at the Indian Ocean (75–95°E, 5°S-5°N averaged) reference point.

200-hPa zonal wind, and OLR in the CEOF analysis. In other respects our approach largely follows theirs.

Figure 5 shows the leading pair of CEOFs derived from observations and each simulation. The CEOFs are arranged to have similar patterns to those of *Wheeler and Hendon* [2004] so that the definitions of phases used in the MJO life-cycle composite below are consistent to those from observations. In Figure 5, the top panels represent a mode



Journal of Advances in Modeling Earth Systems 2011ms000081.3d 28/11/11 16:42:11
*The Charlesworth Group*, Wakefield +44(0)1924 369598 - Rev 7.51n/W (Jan 20 2003)

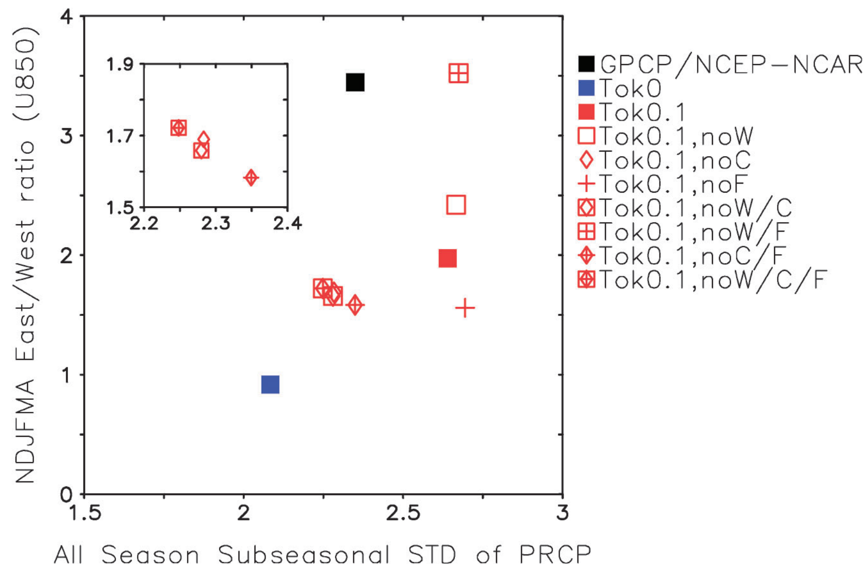


**Figure 4.** Scatterplot of standard deviation of precipitation averaged over 0–360°E, 30°S-30°N and eastward/westward ratio of 850-hPa zonal wind. The eastward/westward ratio is defined as the ratio of eastward propagating spectral power (summation over wavenumber 1–3, period 30–70 day) to its westward propagating counterpart. Closed squares show observations (black), Tok0 (blue), and Tok0.1 (red). Open square, open diamond, and cross symbols represent simulations without WISHE, CRI, and FWC, respectively. Combinations of open and cross symbols indicate double or triple mechanism denial experiments.

with negative (positive) OLR anomalies in the Indian Ocean (western Pacific), while convective anomalies appear in the Maritime continent in the lower panel (a counterpart mode to that in the upper panel). In both modes convective anomalies are accompanied by a deep baroclinic structure in upper- and lower-tropospheric zonal wind. The CEOFs in all of the simulations capture the gross features of the leading mode in observations, such as the location of the maximum in convection (minimum OLR), baroclinic wind structure, and planetary spatial scale. Therefore, we regard these pairs of modes as representative of the MJO simulated in each simulation in the following analysis and discussions.

In Figure 5, the numbers in each box represent the percentage of the variance explained by each mode (%VAR), while the numbers above upper box show the mean coherence squared between two PCs over the 30-80-day period range ($Coh^2$). In Table 2, these numbers as derived from observations and all simulations are shown for quantitative comparison of the characteristics of the MJOs. %VAR represents the degree of dominance of the MJO mode over other sub-seasonal time scale variability, while $Coh^2$ is a metric for coherent eastward propagation of the MJO mode. %VAR and $Coh^2$ from the simulations are smaller than that observed, as in simulations with other GCMs [*Kim et al.*, 2009]. Turning off CRI (with the other mechanisms fixed) tends to reduce both metrics above, implying that CRI induces a more dominant, more coherent eastward propagating MJO mode (Tok0.1 vs. noC, noW vs. noW/C, noF vs. noC/F, and noW/F vs. noW/C/F). When CRI is active, switching off WISHE makes all metrics higher than those in the counter experiments (Tok0.1 vs. noW and noF vs. noW/F). This again suggests that WISHE has negative impacts on the MJO mode in this model. FWC seems to have no systematic impacts in the metrics of the MJO mode.

To assess whether the extracted MJO modes are physically meaningful and distinct from a red noise process, and to examine the temporal period associated with each CEOF, we calculate power spectra of the associated unfiltered PCs. The unfiltered PCs are obtained by projecting the leading CEOFs in Figure 5 onto unfiltered anomaly data with only the seasonal cycle removed. If the power spectra of the unfiltered PCs shown in Figure 6 yield statistically significant peaks at MJO time scales, then we have increased confidence that the extracted MJO modes are physically meaningful. The percentage of power residing within the 30-80-day period range to the total in the spectrum (%30–80 d) is given in each panel to quantify the dominance of time scale of the MJO observed.

In observations (Figure 6a), statistically significant spectral power at the 99% confidence level relative to a red noise process is concentrated at periods of 30 to 80 days. Tok0.1 (Figure 6b) also has statistically significant spectral power at MJO time scales, although it is shifted a bit to higher frequency relative to observations. On contrast, there is no such signal in Tok0 (Figure 6f). Figure 6 shows that turning off CRI always reduces power at MJO time scales and enhances power at shorter period (Tok0.1 vs. noC, noW vs. noW/C, noF vs. noC/F, and noW/F vs. noW/C/F). The statistically significant power at MJO time scales is enhanced without WISHE in simulations in which CRI is turned on



**Journal of Advances in Modeling Earth Systems 2011ms000081.3d** 28/11/11 16:42:28
*The Charlesworth Group*, Wakefield +44(0)1924 369598 - Rev 7.51n/W (Jan 20 2003)

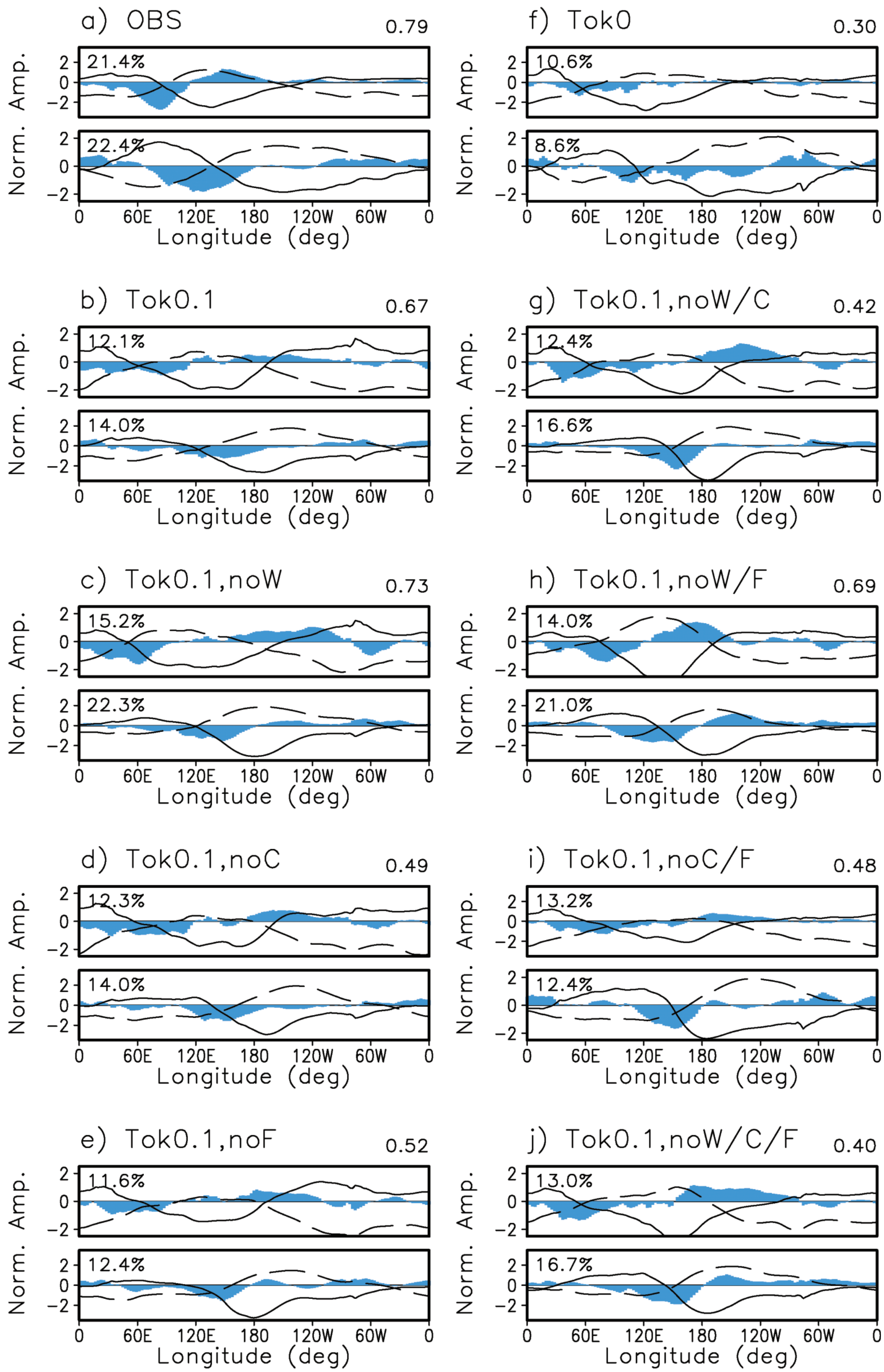


**Figure 5.** First two CEOF modes of 20–100-day 15°S–15°N averaged 850-hPa and 200-hPa zonal wind and OLR. The total variance explained by each mode is shown in the top left of each panel. The mean coherence squared between principal components of two modes within a 30–80-day period is given above the upper panel. The sign and location (upper or lower) of each mode are arbitrarily adjusted to be similar to observations. The mode having the largest percentage variance explained is the first mode. The leading pair of modes is separated from the 3rd mode by *North et al.*'s [1982] criterion in all observations and all simulations except for Tok0.



**Journal of Advances in Modeling Earth Systems 2011ms000081.3d** 28/11/11 16:42:33
*The Charlesworth Group*, Wakefield +44(0)1924 369598 - Rev 7.51n/W (Jan 20 2003)

**Table 2.** MJO Metrics Derived From CEOF Analysis[a]

| | OBS | Tok0.1 | No W | No C | No F | No W/C | No W/F | No C/F | No W/C/F |
|---|---|---|---|---|---|---|---|---|---|
| %VAR | 43.8 | 26.1 | 37.5 | 26.3 | 24.0 | 29.0 | 35.0 | 25.6 | 29.7 |
| $Coh^2$ | 0.79 | 0.67 | 0.73 | 0.49 | 0.52 | 0.42 | 0.69 | 0.48 | 0.40 |
| %30-80 d | 58.1 | 42.7 | 45.6 | 30.6 | 34.8 | 32.4 | 42.6 | 30.7 | 29.3 |

[a]%VAR: percentage variance explained by the first leading pair of CEOF (Figure 5). $Coh^2$: coherence squared between two PCs of leading pair of CEOF within 30–80 day period (Figure 5). %30–80 d: percentage of power residing within 30–80 day period to total in power spectrum of unfiltered PC (1st mode, Figure 6).

(Tok0.1 vs. noW and noF vs. noW/F). The values of %30–80 d in Table 2 imply similar conclusions.

### 3.3. Life-Cycle Composites and Process Diagnostics

In this subsection we present diagnostics aimed more directly at illuminating the macroscopic mechanisms of interest (WISHE, CRI, FWC). For this purpose, MJO life-cycle composites [*Wheeler and Hendon*, 2004] of OLR, evaporation, 1000-hPa zonal wind, specific humidity, and 925-hPa moisture convergence are constructed. The MJO life-cycle composites are constructed by averaging 20-100-day bandpass filtered anomalies across all days that fall within a given phase when the MJO amplitude $[(PC1^2+PC2^2)^{1/2}]$ is greater or equal to 1. The 8 phases are determined in the two-dimensional space of PCs from CEOF analysis. Readers are referred to *Wheeler and Hendon* [2004] and *Kim et al.* [2009] for more details of the procedures used to calculate the MJO life cycle composite and their application to climate model simulations.

#### 3.3.1. NoWISHE Experiments

Figure 7 shows MJO life cycle composites of 10°S-10°N averaged OLR (contours) and evaporation (shaded) anomalies. The observed latent heat flux anomaly related to the MJO mode slightly lags, but to a significant extent is in phase with the convection (negative OLR anomaly), as shown in Figure 7a. This suggests that the latent heat flux anomalies act to reinforce the convective anomalies in the active phase of the MJO. The simulations without WISHE do show small evaporation anomalies associated with the MJO; these result from evaporation over land where it remains interactive. In Tok0.1, contrary to observations, the surface latent heat flux and convection (negative OLR) anomalies are mostly anti-correlated in the region near the largest MJO-related convective anomalies. This is consistent with the result above that WISHE damps the MJO-related convective anomalies in the control simulations. The reason for the anti-correlation between latent heat flux and OLR appears to stem from the phase relationship between low level wind and convection, which is different from that found in observations. Surface (1000 hPa) westerlies, which lag convection but are partly in phase with it in observations, are much weaker in Tok0.1 than in observations, particularly in the region west of 120E where the MJO is growing (Figure 8). At the same time, easterly anomalies are more nearly in phase with enhanced convection than in observations. Since the mean wind is westerly in the regions of MJO-related convection, westerly anomalies correspond to greater surface wind speed (and thus flux) and easterlies to weaker wind speed and flux. Thus the destructive effect of surface latent heat flux on the simulated MJO - shown above by the increases in %VAR, $Coh^2$, and %30–80 d of the simulated MJO mode when WISHE is disabled (as long as CRI remains active) – appear to be caused by an incorrect simulation of the phase relationship between convection and low level wind in the control.

In Figure 9, MJO life-cycle composites of 10°S-10°N averaged specific humidity are displayed in a longitude-height cross section (upper), together with 10°S-10°N averaged OLR anomaly (lower). A specific phase, in which the MJO-related convective anomalies are located near the Maritime continent, is picked in each case for comparison. Clearly the experiments that simulate strong MJO signal without WISHE, but with CRI (noW and noW/F), show stronger moisture anomalies than do the other runs, especially at near-surface levels. This is consistent with the expectation that convective activity is stronger as moist static energy in the planetary layer increases. Regarding the destructive effect of WISHE on the convective anomalies, we speculate that removing WISHE helps the model to retain strong moisture anomalies near the surface, by removing the impact of surface wind speed and latent heat flux changes which otherwise would be anticorrelated with those moisture anomalies.

#### 3.3.2. NoCRI Experiments

Contrary to the impact of WISHE, excluding CRI weakens the moisture signal in the MJO life-cycle composite, particularly near and below 900 hPa (e.g., noC, and noC/F in Figure 9). Similarly, without CRI, the changes in the strength and period of the simulated MJO are in the opposite direction to those obtained when WISHE is turned off.

Figure 10 shows composites of the negative of the OLR anomaly with respect to the precipitation anomaly. Here precipitation is expressed in units of vertically-integrated condensational heating rate (W $m^{-2}$), the same as those of OLR. These are not composites with respect to the MJO, but simply composites of daily-mean (negative) OLR based on daily-mean precipitation at each grid point. The negative of the OLR approximates the column integrated net radiative



**Journal of Advances in Modeling Earth Systems 2011ms000081.3d** 28/11/11 16:42:45
*The Charlesworth Group*, Wakefield +44(0)1924 369598 - Rev 7.51n/W (Jan 20 2003)

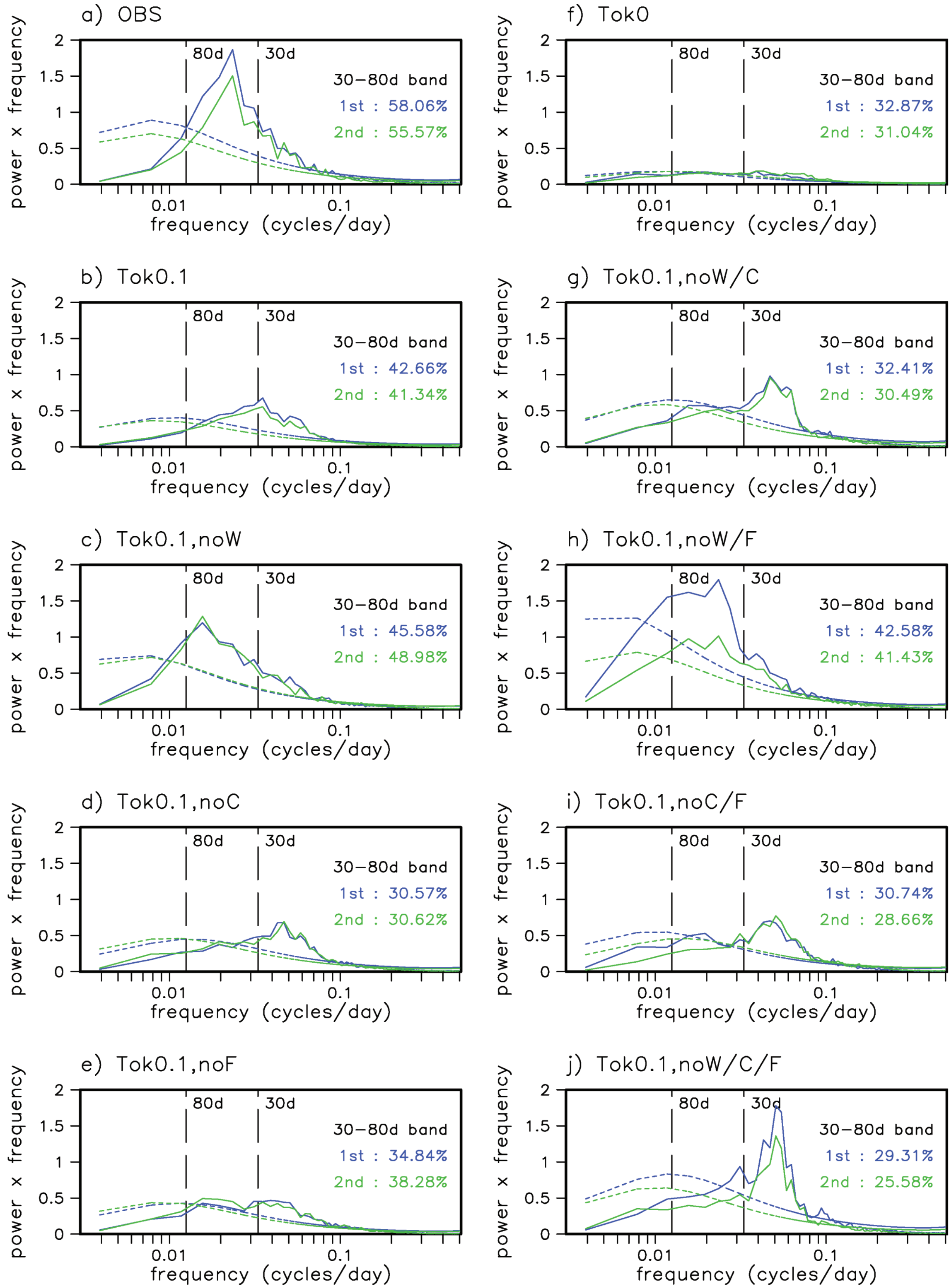


**Figure 6.** The power spectrum of the unfiltered PC derived by projecting the CEOFs onto unfiltered data (seasonal cycle removed): first mode (blue) and second mode (green). Dashed lines show the 99% confidence limit for a red noise spectrum.



Journal of Advances in Modeling Earth Systems 2011ms000081.3d 28/11/11 16:42:46
*The Charlesworth Group*, Wakefield +44(0)1924 369598 - Rev 7.51n/W (Jan 20 2003)

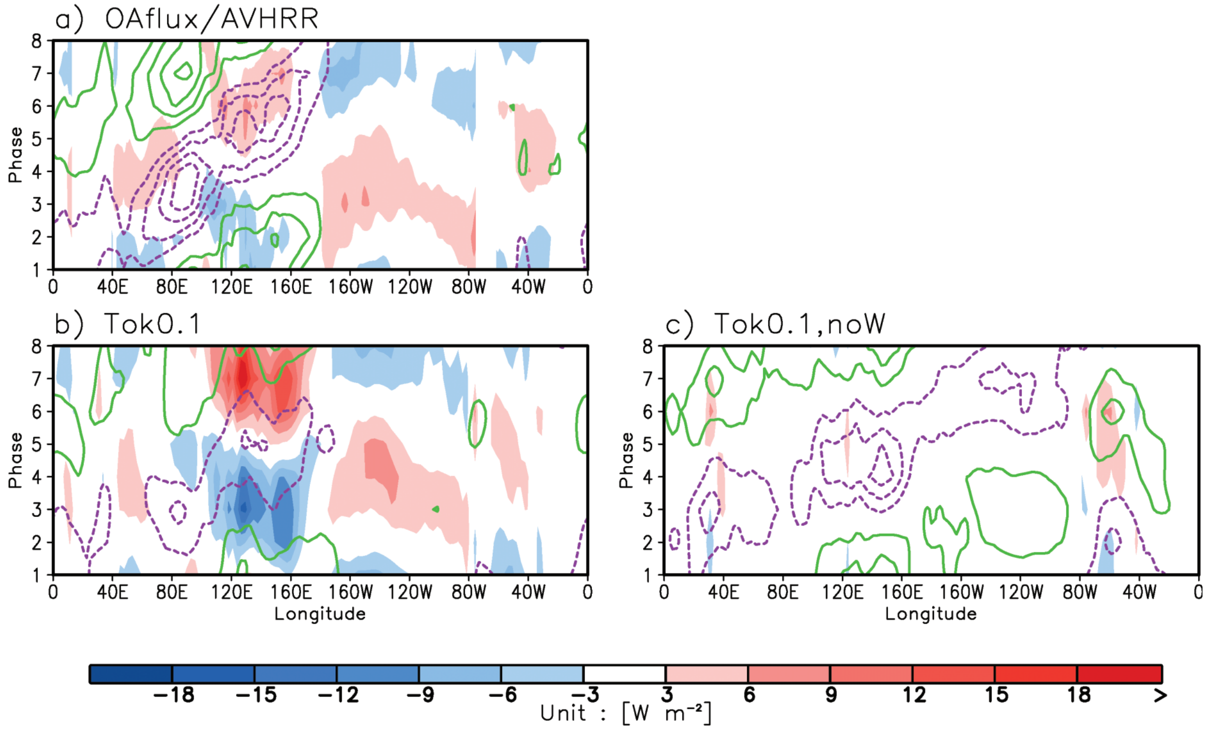


**Figure 7.** Phase–longitude diagram of OLR (contour plotted every 5 W m$^{-2}$, positive (green) and negative (purple)) and surface latent heat flux (W m$^{-2}$, shaded). Phases are from the MJO life cycle composite with values averaged between 10°S and 10°N. (a) OAflux/AVHRR, (b) Tok0.1, and (c) Tok0.1,noW.

heating anomaly, assuming that surface longwave fluxes do not vary significantly. The slope of the curve (a dimensionless number) can be considered a linearized measure of the cloud-radiative feedback on convection; for a given amount of convective heating, the slope tells us how much additional heating of the column occurs due to the greenhouse effect of the clouds [e.g., *Su and Neelin*, 2002; *Fuchs and Raymond*, 2002; *Bretherton and Sobel*, 2002; *Lin and Mapes*, 2004). The composites based on observations show that the positive feedback from radiative heating is above 20% (a slope of 0.2) when the precipitation anomaly is small (less than about 4 mm day$^{-1}$), and above 10% until the precipitation anomaly reaches about 14 mm day$^{-1}$ (about 200 W m$^{-2}$). In Tok0.1, the radiative feedback is stronger than that observed, especially when the rainfall anomaly is small: it is greater than 20% for precipitation anomalies less than 8 mm day$^{-1}$, and greater than 10% for precipitation anomalies up to 22 mm day$^{-1}$. This does not by itself illuminate the details of the mechanism by which CRI amplifies the MJO (as opposed to other disturbances with different space or time scales), but the presence of a strong CRI feedback in the model is at least consistent with an

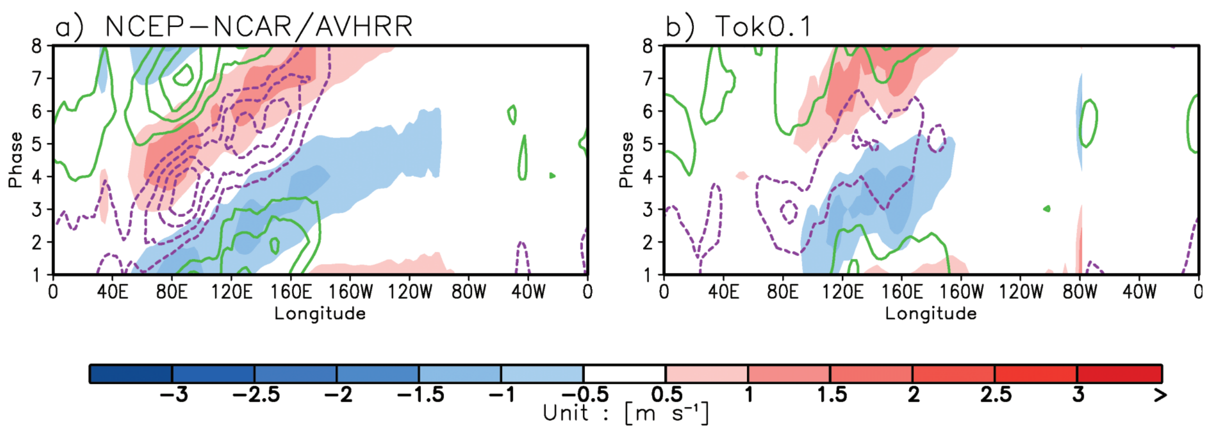


**Figure 8.** Same as Figure 7, except for 1000 hPa zonal wind and OLR. (a) NCEP-NCAR/AVHRR and (b) Tok0.1.



**Journal of Advances in Modeling Earth Systems 2011ms000081.3d** 28/11/11 16:42:59
*The Charlesworth Group*, Wakefield +44(0)1924 369598 - Rev 7.51n/W (Jan 20 2003)

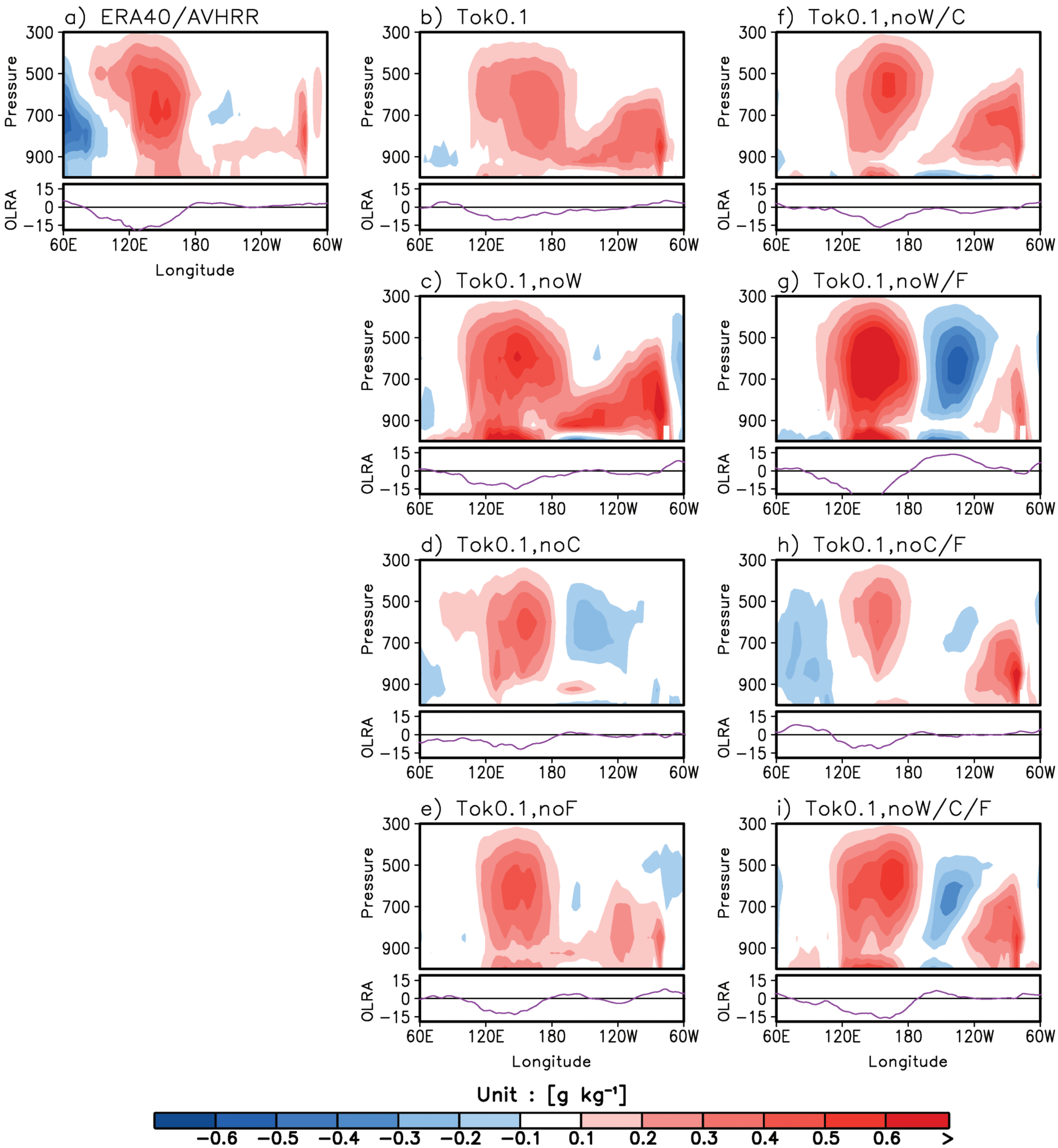


**Figure 9.** MJO life-cycle composite of 20–100 day bandpass filtered, 10°S-10°N averaged specific humidity anomaly (upper panel), and filtered, 10°S-10°N averaged OLR anomaly (lower panel) at different phases in which the convective anomaly is located near the Maritime continent. (a) GPCP/NCEP-NCAR, (b) Tok0.1, (c) Tok0.1,noW, (d) Tok0.1,noC, (e) Tok0.1,noF, (f) Tok0.1,noW/C, (g) Tok0.1,noW/F, (h) Tok0.1,noC/F, and (i) Tok0.1,noW/C/F.

important role for that process in the simulated MJO dynamics.

The strength of the convectively coupled Kelvin wave (CCKW) is also influenced by CRI, but in the opposite way to that of the MJO. Figure 11 shows the symmetric wave-number-frequency power spectra (normalized by estimated background power [*Wheeler and Kiladis*, 1999]) of equatorial precipitation from observation and two selected experiments,



Journal of Advances in Modeling Earth Systems 2011ms000081.3d 28/11/11 16:43:10
*The Charlesworth Group*, Wakefield +44(0)1924 369598 - Rev 7.51n/W (Jan 20 2003)

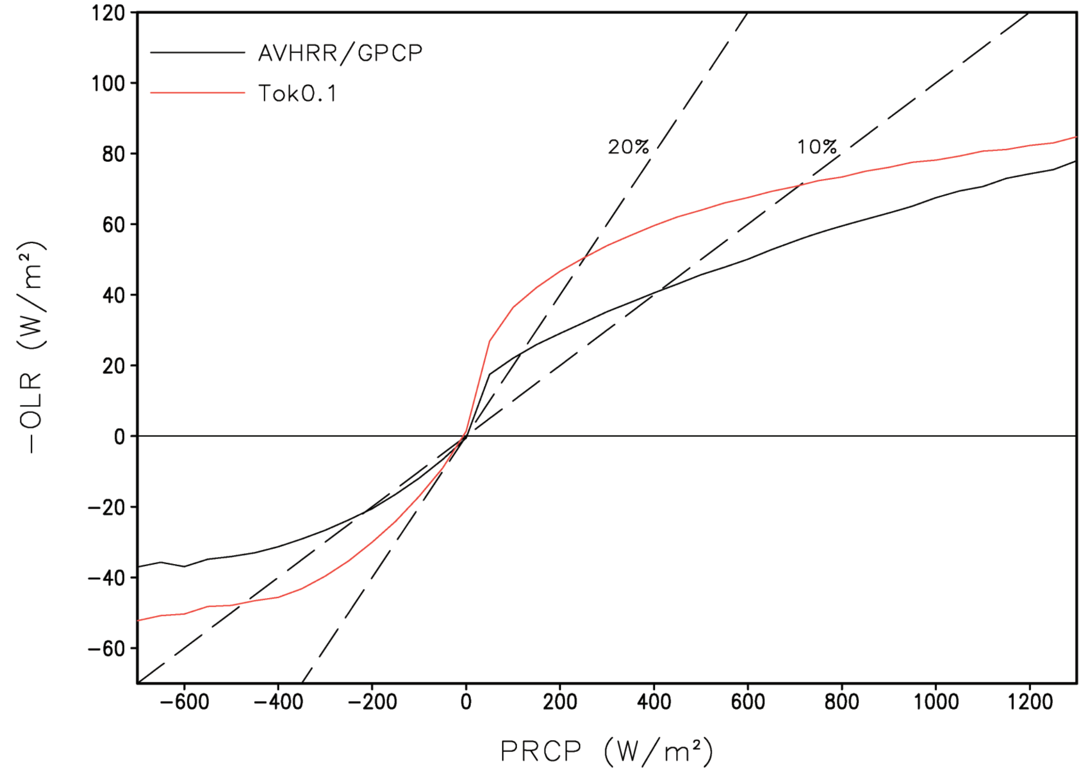


**Figure 10.** Negative OLR anomaly (W $m^{-2}$) composited based on precipitation (W $m^{-2}$). The unit of precipitation in this plot is converted to condensational heating rate. Points over the warm pool region (40–180°E, 20°S-20°N) are used in calculations. Solid lines represent observations (black) and Tok0.1 (red). The two black dashed lines show 10% and 20% of precipitation, respectively.

noW/C/F and noW/F. In observations (Figure 11a), the power in the CCKW and convectively coupled equatorial Rossby wave bands (with equivalent depth of 25 m) as well as in the MJO band (wavenumber 1–3, period 30–60 days) are distinguished from the background spectrum. A strong CCKW signal is prominent in noW/C/F (Figure 11b). When compared to noW/C/F, noW/F has a much weaker CCKW signal, but the MJO is much stronger.

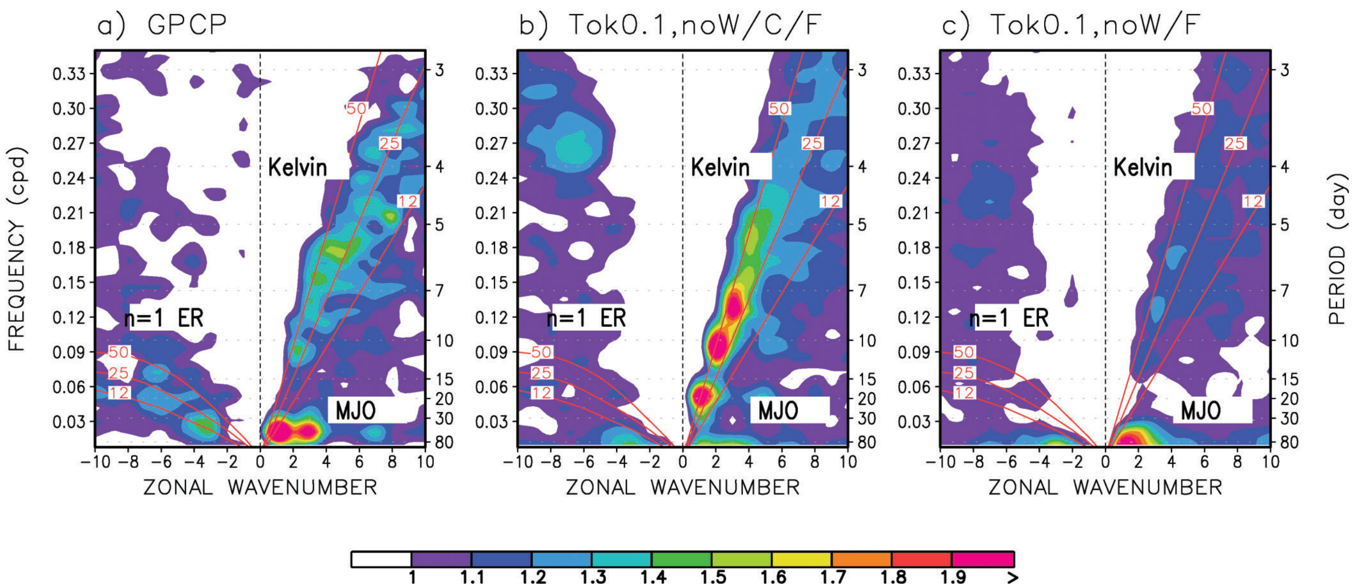


**Figure 11.** Space–time spectrum of the 15°N–15°S symmetric component of precipitation divided its estimated background spectrum. (a) GPCP, (b) Tok0.1,noW/C/F, and (c) Tok0.1,noW/F. Superimposed are the dispersion curves of the odd meridional mode numbered equatorial waves for the equivalent depths of 12, 25, and 50 m.



**Journal of Advances in Modeling Earth Systems 2011ms000081.3d** 28/11/11 16:43:24
*The Charlesworth Group*, Wakefield +44(0)1924 369598 - Rev 7.51n/W (Jan 20 2003)

We define a metric for the CCKW by the ratio of spectral power over the CCKW band (summation over wavenumbers 1–14 and periods between 2.5–30 days, within dispersion curves with equivalent depths of 8 m and 90 m) to the background power, and make a scatter plot of that metric and the %30–80 d metric (Figure 12). In the scatter plot, we see that the CCKW gets stronger when we turn-off CRI. Additionally, the stronger Kelvin wave is accompanied by a reduction in the %30–80 d metric, indicating a shortening of the period of the MJO. We speculate that these are different manifestation of the same phenomenon. Since some CCKW variance is within the 20–100 day band and has broadly similar spatial structure to the MJO, the decrease in the MJO period may be in part due to an increased projection of the CCKW onto the combined EOF pattern whose principal components are used to define the MJO spectrum. As the CCKWs tend to have higher frequency than the MJO, this reduces the apparent MJO period as determined (for example) by the %30–80 d metric.

### 3.3.3. NoFWC Experiments

Figure 13 shows MJO life-cycle composites of 10°S-10°N averaged 925 hPa moisture convergence and OLR anomalies. In observations, the positive PBL moisture convergence anomaly slightly leads the convection anomaly (Figure 13a). The expectation when we turn off FWC is that the phase difference between convection and PBL moisture convergence should disappear. This is because, in FWC theory, the PBL moisture convergence is frictionally driven ahead (east) of convection where easterly surface wind anomalies exist as the Kelvin wave response to the current convection (heating). Absent this frictional

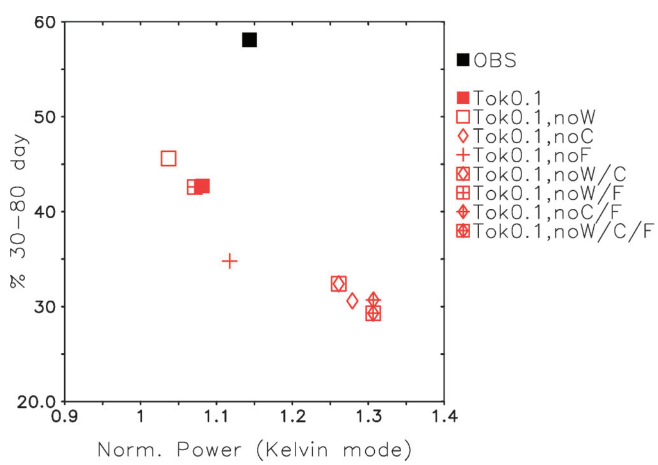


**Figure 12.** Scatterplot of the metric for the convectively coupled Kelvin wave and %30–80 d defined in Table 2. The convectively coupled Kelvin wave metric is defined as a ratio of spectral power over the Kelvin wave band (summation over wavenumber 1–14, period 2.5–30 day, within dispersion curves with equivalent depths of 8 m and 90 m) to that of background power. The meaning of symbols is same as in Figure 4.

component to the convergence, we expect surface convergence - like low-level convergence in general - to be at least approximately collocated with the strongest convection, consistent with large-scale ascent via the mass budget. When we compare Tok0.1 to noF, indeed the phase difference between convergence and convection is reduced without interactive wind stress. Anomalous 925-hPa moisture convergence is nearly in phase with negative OLR in the noF run (Figure 13c) while the negative OLR anomaly slightly lags moisture convergence in Tok0.1 (Figure 13b) as in observations. However, prescribing wind stress does not strongly alter the boundary layer and lower tropospheric specific humidity anomalies (Figure 9) compared to Tok0.1. This might be why the MJO is not greatly weakened when FWC is disabled. It seems that frictional convergence is not a critically important mechanism for the development or maintenance of the MJO in this particular model.

## 4. Conclusions

In this study, we have conducted a series of Madden-Julian oscillation (MJO) mechanism-denial experiments using the SNU AGCM. A version of the AGCM in which the convective scheme has been tuned to improve the simulation of the MJO was used to investigate the relative importance of several macroscopic mechanisms to the resulting simulated MJO. Daily climatological seasonal cycles of i) surface latent heat flux, ii) net radiative heating rate, and iii) surface wind stress were obtained from a control simulation and prescribed in the mechanism-denial experiments to turn off i) surface turbulent flux feedbacks (WISHE), ii) cloud-radiative feedbacks (CRI), and iii) frictional wave-CISK (FWC), respectively. The difference in the simulated intraseasonal variability (ISV) between two simulations in which a given process is or is not disabled while the others are held fixed (either on or off) is taken as a measure of the importance of that process to the simulated ISV. Gross metrics of ISV, such as total variance of key fields in the 20–100 band and the ratio of eastward- to westward-propagating variance, are considered, as well as standard diagnostics more specifically designed to isolate each simulation's version of the MJO.

The results indicate that both CRI and WISHE are important to the simulated MJO in this model, while FWC is less important. To the extent that we consider this model relevant to reality, these results are consistent with *Sobel et al.* [2008, 2010] that presented evidence from observations and models that WISHE and CRI are important to the MJO. On the other hand, while the effect of CRI on the MJO is positive in this model, that of WISHE is negative, contrary to the arguments of *Sobel et al.* [2008, 2010] as well as to the original WISHE theories [*Emanuel*, 1987; *Neelin et al.*, 1987]. On the other hand again, however, the negative impact of WISHE in this model was shown above to result from an unrealistic simulation of the phase relationship between precipitation and surface winds in the control simulation, with the surface easterly anomalies being



Journal of Advances in Modeling Earth Systems 2011ms000081.3d 28/11/11 16:43:41
The Charlesworth Group, Wakefield +44(0)1924 369598 - Rev 7.51n/W (Jan 20 2003)

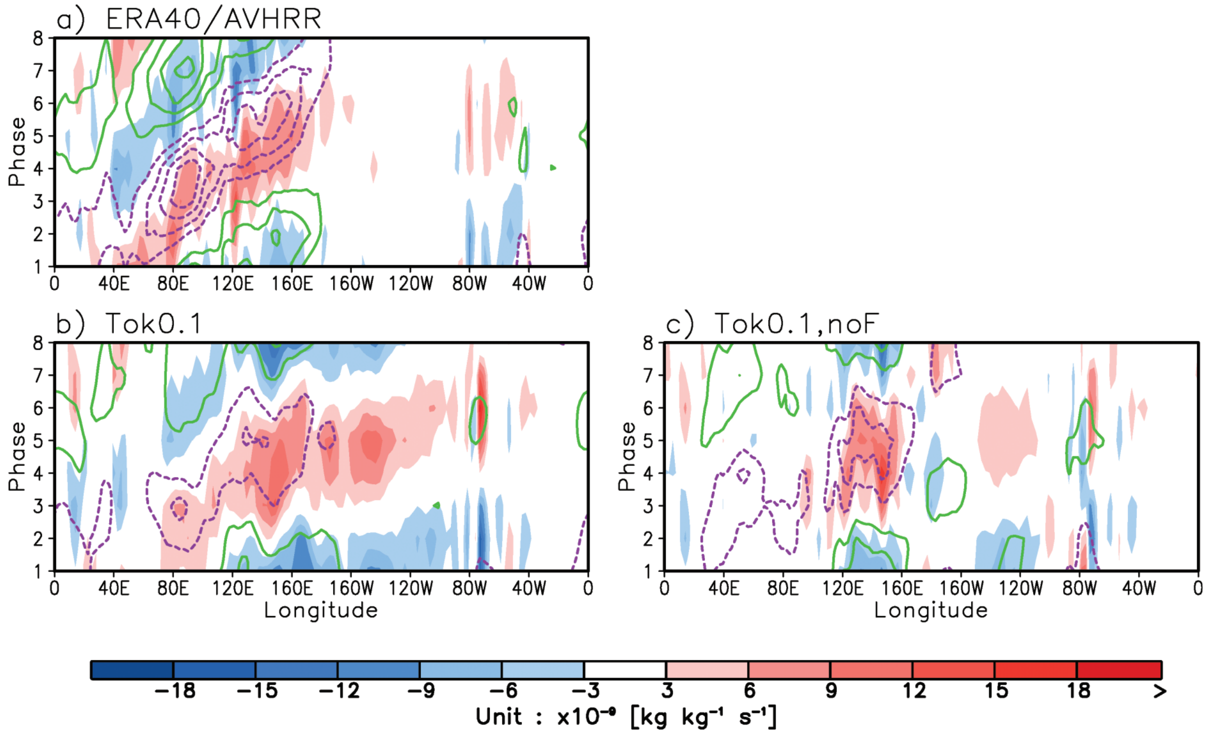


**Figure 13.** As in Figure 8 but for 925-hPa moisture convergence (kg $kg^{-1}$ $s^{-1}$). (a) ERA40/AVHRR, (b) Tok0.1, and (c) Tok0.1,noF.

shifted too far west (thus too much in phase with enhanced convection) while the surface westerly anomalies are too weak and also too far west (and thus too far out of phase with convection). Because of this we do not consider the results here to be evidence against the relevance of WISHE to the real MJO.

In the control model, the cloud-radiative feedback, quantified by the mean relationship on daily timescales at individual grid-points between column-integrated convective and radiative heating, is stronger than that found observations, particularly when anomalous precipitation is small. Thus it is possible that CRI plays too large a positive role in the MJO in this model, while WISHE plays much too negative a role. A systematic relationship between MJO and the convectively coupled Kelvin wave (CCKW) was also found in this study. When CRI is turned off, the CCKW gets stronger preferentially so that the amplitude and period of the MJO becomes weaker and shorter. Therefore, the CCKW and MJO are not entirely independent from each other in this model.

When FWC is turned off, the phase difference between convection and PBL moisture convergence is reduced, as expected. However, neither boundary layer nor lower tropospheric specific humidity anomalies nor the amplitude of the MJO overall is weakened much by the disabling of FWC. It appears that frictional convergence is not a dominant mechanism for the MJO in this particular model, consistent with the results of *Chao and Chen* [2001] who used a different model.

All these results may well be model-dependent. The great advantage of mechanism denial experiments in numerical models is that they give relatively clear information about which mechanisms are important in the model. The great disadvantage is that any model, certainly including this one, is flawed. It would be useful to the broader effort to understand the MJO if other investigators would perform similar experiments to evaluate the relevance of these mechanisms – as well as any others which can be tested in this manner – in other models, as proposed by *Sobel et al.* [2010].

**Acknowledgments.** This work was supported by NASA grant NNX09AK34G and NOAA grant NA08OAR4320912. DK and ISK were also supported by the National Research Foundation of Korea (NRF) Grant Funded by the Korean Government (MEST) (NRF-2009-C1AAA001-2009-0093042) and second phase of the Brain Korea 21.

## References

Arakawa, A., and W. H. Schubert (1974), Interaction of a cumulus cloud ensemble with the large-scale environment, part I, *J. Atmos. Sci.*, *31*, 674–701, doi:10.1175/1520-0469(1974)031<0674:IOACCE>2.0.CO;2.

Benedict, J. J., and D. A. Randall (2009), Structure of the Madden-Julian Oscillation in the superparameterized CAM, *J. Atmos. Sci.*, *66*, 3277–3296, doi:10.1175/2009JAS3030.1.

Bergman, J. W., H. H. Hendon, and K. M. Weickmann (2001), Intraseasonal air-sea interactions at the onset of



**Journal of Advances in Modeling Earth Systems 2011ms000081.3d** 28/11/11 16:43:45
*The Charlesworth Group*, Wakefield +44(0)1924 369598 - Rev 7.51n/W (Jan 20 2003)

El Niño, *J. Clim.*, *14*, 1702–1719, doi:10.1175/1520-0442(2001)014<1702:IASIAT>2.0.CO;2.

Bessafi, M., and M. C. Wheeler (2006), Modulation of south Indian Ocean tropical cyclones by the Madden-Julian Oscillation and convectively coupled equatorial waves, *Mon. Weather Rev.*, *134*, 638–656, doi:10.1175/MWR3087.1.

Bonan, G. B. (1996), A land surface model (LSM version 1.0) for ecological, hydrological, and atmospheric studies: Technical description and user's guide, Clim. and Global Dyn. Div., Natl. Cent. for Atmos. Res., Boulder, Colo.

Bretherton, C. S., and A. H. Sobel (2002), A simple model of a convectively-coupled Walker circulation using the weak temperature gradient approximation, *J. Clim.*, *15*, 2907–2920, doi:10.1175/1520-0442(2002)015<2907:ASMOAC>2.0.CO;2.

Chao, W. C., and B. D. Chen (2001), The role of surface friction in tropical intraseasonal oscillation, *Mon. Weather Rev.*, *129*, 896–904, doi:10.1175/1520-0493(2001)129<0896:TROSFI>2.0.CO;2.

Emanuel, K. A. (1987), An air-sea interaction-model of intraseasonal oscillations in the tropics, *J. Atmos. Sci.*, *44*, 2324–2340, doi:10.1175/1520-0469(1987)044<2324:AASIMO>2.0.CO;2.

Fuchs, Z., and D. J. Raymond (2002), Large-scale modes of a nonrotating atmosphere with water vapor and cloud-radiation feedbacks, *J. Atmos. Sci.*, *59*, 1669–1679, doi:10.1175/1520-0469(2002)059<1669:LSMOAN>2.0.CO;2.

Fuchs, Z., and D. J. Raymond (2005), Large-scale modes in a rotating atmosphere with radiative-convective instability and WISHE, *J. Atmos. Sci.*, *62*, 4084–4094, doi:10.1175/JAS3582.1.

Fuchs, Z., and D. J. Raymond (2007), A simple, vertically resolved model of tropical disturbances with a humidity closure, *Tellus, Ser. A*, *59*, 344–354, doi:10.1111/j.1600-0870.2007.00230.x.

Grabowski, W. W. (2003), MJO-like coherent structures: Sensitivity simulations using the cloud-resolving convection parameterization (CRCP), *J. Atmos. Sci.*, *60*, 847–864, doi:10.1175/1520-0469(2003)060<0847:MLCSSS>2.0.CO;2.

Hendon, H. H., and M. L. Salby (1994), The life-cycle of the Madden-Julian Oscillation, *J. Atmos. Sci.*, *51*, 2225–2237, doi:10.1175/1520-0469(1994)051<2225:TLCOTM>2.0.CO;2.

Holtslag, A. A. M., and B. A. Boville (1993), Local versus nonlocal boundary-layer diffusion in a global climate model, *J. Clim.*, *6*, 1825–1842, doi:10.1175/1520-0442(1993)006<1825:LVNBLD>2.0.CO;2.

Hu, Q., and D. A. Randall (1994), Low-frequency oscillations in radiative-convective systems, *J. Atmos. Sci.*, *51*, 1089–1099, doi:10.1175/1520-0469(1994)051<1089:LFOIRC>2.0.CO;2.

Hu, Q., and D. A. Randall (1995), Low-frequency oscillations in radiative convective systems. Part II: An idealized model, *J. Atmos. Sci.*, *52*, 478–490, doi:10.1175/1520-0469(1995)052<0478:LFOIRC>2.0.CO;2.

Huffman, G. J., R. F. Adler, M. M. Morrissey, D. T. Bolvin, S. Curtis, R. Joyce, B. McGavock, and J. Susskind (2001), Global precipitation at one-degree daily resolution from multisatellite observations, *J. Hydrometeorol.*, *2*, 36–50, doi:10.1175/1525-7541(2001)002<0036:GPAODD>2.0.CO;2.

Inness, P. M., J. M. Slingo, E. Guilyardi, and J. Cole (2003), Simulation of the Madden-Julian Oscillation in a coupled general circulation model. Part II: The role of the basic state, *J. Clim.*, *16*, 365–382, doi:10.1175/1520-0442(2003)016<0365:SOTMJO>2.0.CO;2.

Jones, C., and B. C. Weare (1996), The role of low-level moisture convergence and ocean latent heat fluxes in the Madden and Julian Oscillation: An observational analysis using ISCCP data and ECMWF analyses, *J. Clim.*, *9*, 3086–3104, doi:10.1175/1520-0442(1996)009<3086:TROLLM>2.0.CO;2.

Kalnay, E., *et al.*, (1996), The NCEP/NCAR 40-year reanalysis project, *Bull. Am. Meteorol. Soc.*, *77*, 437–471, doi:10.1175/1520-0477(1996)077<0437:TNYRP>2.0.CO;2.

Kessler, W. S. (2001), EOF representations of the Madden-Julian Oscillation and its connection with ENSO, *J. Clim.*, *14*, 3055–3061, doi:10.1175/1520-0442(2001)014<3055:EROTMJ>2.0.CO;2.

Kessler, W. S., M. J. McPhaden, and K. M. Weickmann (1995), Forcing of intraseasonal Kelvin waves in the equatorial Pacific, *J. Geophys. Res.*, *100*, 10,613–10,631., doi:10.1029/95JC00382.

Kim, D., *et al.*, (2009), Application of MJO simulation diagnostics to climate models, *J. Clim.*, *22*, 6413–6436, doi:10.1175/2009JCLI3063.1.

Kim, D., A. H. Sobel, D. M. W. Frierson, E. D. Maloney, and I.-S. Kang (2011), A Systematic relationship between intraseasonal variability and mean state bias in AGCM simulations, *J. Clim.*, *24*, 5506–5520, doi:10.1175/2011JCLI4177.1.

Lau, K. M., and P. H. Chan (1988), Intraseasonal and interannual variations of tropical convection—A possible link between the 40–50 day oscillation and ENSO, *J. Atmos. Sci.*, *45*, 506–521, doi:10.1175/1520-0469(1988)045<0506:IAIVOT>2.0.CO;2.

Lau, N. C., and K. M. Lau (1986), The structure and propagation of intraseasonal oscillations appearing in a GFDL general circulation model, *J. Atmos. Sci.*, *43*, 2023–2047, doi:10.1175/1520-0469(1986)043<2023:TSAPOI>2.0.CO;2.

Lau, K. M., and L. Peng (1987), Origin of low-frequency (intraseasonal) oscillations in the tropical atmosphere. Part I: Basic theory, *J. Atmos. Sci.*, *44*, 950–972, doi:10.1175/1520-0469(1987)044<0950:OOLFOI>2.0.CO;2.

Le Treut, H., and Z. X. Li (1991), Sensitivity of an atmospheric general circulation model to prescribed SST changes: Feedback effects associated with the simulation of cloud optical properties, *Clim. Dyn.*, *5*, 175–187.

Lee, M. I., I. S. Kang, J. K. Kim, and B. E. Mapes (2001), Influence of cloud-radiation interaction on simulating tropical intraseasonal oscillation with an atmospheric general circulation model, *J. Geophys. Res.*, *106*, 14,219–14,233.

Lee, M. I., I. S. Kang, and B. E. Mapes (2003), Impacts of cumulus convection parameterization on aqua-planet AGCM simulations of tropical intraseasonal variability, *J. Meteorol. Soc. Jpn.*, *81*, 963–992, doi:10.2151/jmsj.81.963.

Liebmann, B., and D. L. Hartmann (1984), An observational study of tropical midlatitude interaction on intraseasonal time scales during winter, *J. Atmos. Sci.*, *41*, 3333–3350, doi:10.1175/1520-0469(1984)041<3333:AOSOTI>2.0.CO;2.

Liebmann, B., and C. A. Smith (1996), Description of a complete (interpolated) outgoing longwave radiation dataset, *Bull. Am. Meteorol. Soc.*, *77*, 1275–1277.

Lin, J. L., and B. E. Mapes (2004), Radiation budget of the tropical intraseasonal oscillation, *J. Atmos. Sci.*, *61*, 2050–2062, doi:10.1175/1520-0469(2004)061<2050:RBOTTI>2.0.CO;2.

Lin, J. L., *et al.*, (2006), Tropical intraseasonal variability in 14 IPCC AR4 climate models. Part I: Convective signals, *J. Clim.*, *19*, 2665–2690, doi:10.1175/JCLI3735.1.

Lin, J. L., M. I. Lee, D. Kim, I. S. Kang, and D. M. W. Frierson (2008), The impacts of convective parameterization and moisture triggering on AGCM-simulated convectively coupled equatorial waves, *J. Clim.*, *21*, 883–909, doi:10.1175/2007JCLI1790.1.

Madden, R. A., and P. R. Julian (1971), Detection of a 40–50 day oscillation in the zonal wind in the tropical Pacific, *J. Atmos. Sci.*, *28*, 702–708, doi:10.1175/1520-0469(1971)028<0702:DOADOI>2.0.CO;2.

Madden, R. A., and P. RJulian (1972), Description of global-scale circulation cells in the tropics with a 40–50 day period, *J. Atmos. Sci.*, *29*, 1109–1123, doi:10.1175/1520-0469(1972)029<1109:DOGSCC>2.0.CO;2.

Maloney, E. D. (2009), The moist static energy budget of a composite tropical intraseasonal oscillation in a climate model, *J. Clim.*, *22*, 711–729, doi:10.1175/2008JCLI2542.1.

Maloney, E. D., and D. L. Hartmann (1998), Frictional moisture convergence in a composite life cycle of the Madden-Julian Oscillation, *J. Clim.*, *11*, 2387–2403, doi:10.1175/1520-0442(1998)011<2387:FMCIAC>2.0.CO;2.

Maloney, E. D., and D. L. Hartmann (2000a), Modulation of eastern North Pacific hurricanes by the Madden-Julian Oscillation, *J. Clim.*, *13*, 1451–1460, doi:10.1175/1520-0442(2000)013<1451:MOENPH>2.0.CO;2.

Maloney, E. D., and D. L. Hartmann (2000b), Modulation of hurricane activity in the Gulf of Mexico by the Madden-Julian Oscillation, *Science*, *287*, 2002–2004, doi:10.1126/science.287.5460.2002.

Maloney, E. D., and D. L. Hartmann (2001), The sensitivity of intraseasonal variability in the NCAR CCM3 to changes in convective parameterization, *J. Clim.*, *14*, 2015–2034, doi:10.1175/1520-0442(2001)014<2015:TSOIVI>2.0.CO;2.

Maloney, E. D., and A. H. Sobel (2004), Surface fluxes and ocean coupling in the tropical intraseasonal oscillation, *J. Clim.*, *17*, 4368–4386, doi:10.1175/JCLI-3212.1.

Matthews, A. J. (2000), Propagation mechanisms for the Madden-Julian Oscillation, *Q. J. R. Meteorol. Soc.*, *126*, 2637–2651, doi:10.1002/qj.49712656902.

Moore, A. M., and R. Kleeman (1999), Stochastic forcing of ENSO by the intraseasonal oscillation, *J. Clim.*, *12*, 1199–1220, doi:10.1175/1520-0442(1999)012<1199:SFOEBT>2.0.CO;2.

Moorthi, S., and M. J. Suarez (1992), Relaxed Arakawa-Schubert—A parameterization of moist convection for general circulation models, *Mon. Weather Rev.*, *120*, 978–1002, doi:10.1175/1520-0493(1992)120<0978:RASAPO>2.0.CO;2.

Nakajima, T., M. Tsukamoto, Y. Tsushima, A. Numaguti, and T. Kimura (1995), Modelling of the radiative process in a AGCM, *Clim. Syst. Dyn. Model.*, *3*, 104–123.

Neelin, J. D., I. M. Held, and K. H. Cook (1987), Evaporation-wind feedback and low-frequency variability in the tropical atmosphere, *J. Atmos. Sci.*, *44*, 2341–2348, doi:10.1175/1520-0469(1987)044<2341:EWFALF>2.0.CO;2.

North, G. R., T. L. Bell, R. F. Cahalan, and F. J. Moeng (1982), Sampling errors in the estimation of empirical orthogonal functions, *Mon. Weather Rev.*, *110*, 699–706, doi:10.1175/1520-0493(1982)110<0699:SEITEO>2.0.CO;2.

Numaguti, A., M. Takahashi, T. Nakajima, and A. Sumi (1995), Development of an atmospheric general circulation model, *Clim. Syst. Dyn. Model.*, *3*, 1–27.

Raymond, D. J. (2001), A new model of the Madden-Julian Oscillation, *J. Atmos. Sci.*, *58*, 2807–2819, doi:10.1175/1520-0469(2001)058<2807:ANMOTM>2.0.CO;2.

Salby, M. L., R. R. Garcia, and H. H. Hendon (1994), Planetary-scale circulations in the presence of climatological and wave-induced heating, *J. Atmos. Sci.*, *51*, 2344–2367, doi:10.1175/1520-0469(1994)051<2344:PSCITP>2.0.CO;2.

Shinoda, T., H. H. Hendon, and J. Glick (1998), Intraseasonal variability of surface fluxes and sea surface temperature in the tropical western Pacific and Indian Oceans, *J. Clim.*, *11*, 1685–1702, doi:10.1175/1520-0442(1998)011<1685:IVOSFA>2.0.CO;2.

Slingo, J. M., *et al.*, (1996), Intraseasonal oscillations in 15 atmospheric general circulation models: Results from an




**Journal of Advances in Modeling Earth Systems 2011ms000081.3d** 28/11/11 16:43:52
*The Charlesworth Group*, Wakefield +44(0)1924 369598 - Rev 7.51n/W (Jan 20 2003)

AMIP diagnostic subproject, *Clim. Dyn.*, *12*, 325–357, doi:10.1007/BF00231106.

Sobel, A. H., and S. Gildor (2003), A simple time-dependent model of SST hot spots, *J. Clim.*, *16*, 3978–3992, doi:10.1175/1520-0442(2003)016<3978:ASTMOS>2.0.CO;2.

Sobel, A. H., E. D. Maloney, G. Bellon, and D. M. Frierson (2008), The role of surface heat fluxes in tropical intraseasonal oscillations, *Nat. Geosci.*, *1*, 653–657, doi:10.1038/ngeo312.

Sobel, A. H., E. D. Maloney, G. Bellon, and D. M. Frierson (2010), Surface fluxes and tropical intraseasonal variability: A reassessment, *J. Adv. Model. Earth Syst.*, *2*, 2., doi:10.3894/JAMES.2010.2.2

Sperber, K. R., J. M. Slingo, P. M. Inness, and W. K. M. Lau (1997), On the maintenance and initiation of the intraseasonal oscillation in the NCEP/NCAR reanalysis and in the GLA and UKMO AMIP simulations, *Clim. Dyn.*, *13*, 769–795, doi:10.1007/s003820050197.

Sperber, K. R., S. Gualdi, S. Legutke, and V. Gayler (2005), The Madden-Julian Oscillation in ECHAM4 coupled and uncoupled general circulation models, *Clim. Dyn.*, *25*, 117–140, doi:10.1007/s00382-005-0026-3.

Stephens, G., P. J. Webster, R. H. Johnson, R. Engelen, and T. L'Ecuyer (2004), Observational evidence for the mutual regulation of the tropical hydrological cycle and tropical sea surface temperatures, *J. Clim.*, *17*, 2213–2224, doi:10.1175/1520-0442(2004)017<2213:OEFTMR>2.0.CO;2.

Su, H., and J. D. Neelin (2002), Mechanisms for tropical Pacific descent anomalies during El Niño, *J. Atmos. Sci.*, *59*, 2694–2712, doi:10.1175/1520-0469(2002)059<2694:TMFTPD>2.0.CO;2.

Takayabu, Y. N., T. Iguchi, M. Kachi, A. Shibata, and H. Kanzawa (1999), Abrupt termination of the 1997–98 El Nino in response to a Madden-Julian Oscillation, *Nature*, *402*, 279–282, doi:10.1038/46254.

Tian, B., D. E. Waliser, E. J. Fetzer, B. H. Lambrigtsen, Y. Yung, and B. Wang (2006), Vertical moist thermodynamic structure and spatial-temporal evolution of the MJO in AIRS observations, *J. Atmos. Sci.*, *63*, 2462–2485, doi:10.1175/JAS3782.1.

Tiedtke, M. (1984), The sensitivity of the time-mean large-scale flow to cumulus convection in the ECMWF model, in *Workshop on Convection in Large-Scale Numerical Models*, pp. 297–316, Eur. Cent. for Medium-Range Weather Forecasts, Reading, U. K.

Tokioka, T., K. Yamazaki, A. Kitoh, and T. Ose (1988), The equatorial 30–60 day oscillation and the Arakawa-Schubert penetrative cumulus parameterization, *J. Meteorol. Soc. Jpn.*, *66*, 883–901.

Uppala, S. M., *et al.*, (2005), The ERA-40 re-analysis, *Q. J. R. Meteorol. Soc.*, *131*, 2961–3012, doi:10.1256/qj.04.176.

Waliser, D. E. (1996), Formation and limiting mechanisms for very high sea surface temperature: Linking the dynamics and the thermodynamics, *J. Clim.*, *9*, 161–188, doi:10.1175/1520-0442(1996)009<0161:FALMFV>2.0.CO;2.

Waliser, D. E. (2006), Intraseasonal Variability, in *The Asian Monsoon*, vol. *844*, edited by B. Wang, pp. 203–257, Springer, Heidelberg, Germany.

Waliser, D. E., K. M. Lau, and J. H. Kim (1999), The influence of coupled sea surface temperatures on the Madden-Julian Oscillation: A model perturbation experiment, *J. Atmos. Sci.*, *56*, 333–358, doi:10.1175/1520-0469(1999)056<0333:TIOCSS>2.0.CO;2.

Wang, B. (1988a), Dynamics of tropical low-frequency waves: An analysis of the moist Kelvin wave, *J. Atmos. Sci.*, *45*, 2051–2065, doi:10.1175/1520-0469(1988)045<2051:DOTLFW>2.0.CO;2.

Wang, B. (1988b), Comments on "An air-sea interaction model of intraseasonal oscillation in the tropics," *J. Atmos. Sci.*, *45*, 3521–3525, doi:10.1175/1520-0469(1988)045<3521:COAIMO>2.0.CO;2.

Wang, B. (2005), Theory, in *Intraseasonal Variability in the Atmosphere- Ocean Climate System*, edited by K. M. Lau and D. E. Waliser, pp. 307–360, Springer, Heidelberg, Germany.

Wang, B., and H. Rui (1990), Dynamics of the coupled moist Kelvin-Rossby wave on an equatorial beta-plane, *J. Atmos. Sci.*, *47*, 397–413, doi:10.1175/1520-0469(1990)047<0397:DOTCMK>2.0.CO;2.

Wang, W., and M. E. Schlesinger (1999), The dependence on convection parameterization of the tropical intraseasonal oscillation simulated by the UIUC 11-layer atmospheric GCM, *J. Clim.*, *12*, 1423–1457, doi:10.1175/1520-0442(1999)012<1423:TDOCPO>2.0.CO;2.

Wheeler, M. C., and H. H. Hendon (2004), An all-season real-time multivariate MJO index: Development of an index for monitoring and prediction, *Mon. Weather Rev.*, *132*, 1917–1932, doi:10.1175/1520-0493(2004)132<1917:AARMMI>2.0.CO;2.

Wheeler, M., and G. N. Kiladis (1999), Convectively coupled equatorial waves: Analysis of clouds and temperature in the wavenumber-frequency domain, *J. Atmos. Sci.*, *56*, 374–399, doi:10.1175/1520-0469(1999)056<0374:CCEWAO>2.0.CO;2.

Wheeler, M. C., and J. L. McBride (2005), Australian-Indonesian monsoon, in *Intraseasonal Variability in the Atmosphere-Ocean Climate System*, edited by W. K. M. Lau and D. E. Waliser, pp. 125–173, Springer, Heidelberg, Germany.

Yasunari, T. (1979), Cloudiness fluctuations associated with the Northern Hemisphere summer monsoon, *J. Meteorol. Soc. Jpn.*, *57*, 227–242.

Yu, L., and R. A. Weller (2007), Objectively analyzed air-sea heat fluxes for the global ice-free oceans (1981–2005),



Journal of Advances in Modeling Earth Systems 2011ms000081.3d 28/11/11 16:43:53
*The Charlesworth Group*, Wakefield +44(0)1924 369598 - Rev 7.51n/W (Jan 20 2003)

*Bull. Am. Meteorol. Soc.*, *88*, 527–539, doi:10.1175/BAMS-88-4-527.

Zhang, C. (2005), The Madden-Julian Oscillation, *Rev. Geophys.*, *43*, RG2003, doi:10.1029/2004RG000158.

Zhang, G. J., and M. Mu (2005), Simulation of the Madden-Julian Oscillation in the NCAR CCM3 using a revised Zhang-McFarlane convection parameterization scheme, *J. Clim.*, *18*, 4046–4064, doi:10.1175/JCLI3508.1.



**Journal of Advances in Modeling Earth Systems 2011ms000081.3d** 28/11/11 16:43:53
*The Charlesworth Group*, Wakefield +44(0)1924 369598 - Rev 7.51n/W (Jan 20 2003)